Assessment of Reynolds-Stress models for aeronautical applications

Gustave Sporschill, Flavien Billard, Michel Mallet, Remi Manceau, Hervé Bézard

Assessment of Reynolds-Stress Models for Aeronautical Applications

Gustave Sporschill[a,b,*], Flavien Billard[a], Michel Mallet[a], Rémi Manceau[b], Hervé Bézard[c]

[a] *Dassault Aviation, Saint-Cloud, France*
[b] *CNRS, Université de Pau et des Pays de l'Adour, E2S UPPA, INRIA, project-team CAGIRE, Laboratory of Mathematics and Applied Mathematics (LMAP), Pau, France*
[c] *ONERA, Toulouse, France*

Abstract

Three Reynolds-Stress Models (RSMs) have been benchmarked on industrial configurations with aeronautical applications. The models are first compared on a zero-pressure-gradient boundary layer, which highlights the differences in the near-wall approaches of the models. Results are then analyzed for the Skåre & Krogstad adverse-pressure-gradient boundary layer and the Common Research Model (CRM) aircraft for two Reynolds numbers. Both cases display improvements in using RSMs over the eddy-viscosity Spalart-Allmaras model. Two of the considered second-moment closures better predict the boundary layer growth and its shape factor in the Skåre & Krogstad test case, and all noticeably improve the drag-due-to-lift in the CRM case.

Keywords: Turbulence modeling, Boundary layer, Turbulence budget, Adverse pressure gradient, Aeronautical applications, Common Research Model

1. Introduction

Turbulence modeling is a key feature of CFD design tools, the improvement of which directly impacts the design margin of aeronautical products. Second-moment closures of the Reynolds-Averaged Navier-Stokes (RANS) equations, also called Reynolds-Stress Models (RSMs), reduce the empiricism of the Eddy-Viscosity Models (EVMs). They inherently render the anisotropy of turbulence for 3D and wall-bounded cases, and are therefore well-adapted to the 3D highly anisotropic flows encountered in aeronautical applications. Their spreading in the industry has mainly suffered for a long time from numerical stiffness. For the last two decades, such models have been developed with emphasis on their robustness in order to be implemented in industrial CFD codes.

Three RSMs are assessed in the present work: the elliptic blending Reynolds-stress model (EB-RSM) (Manceau, 2015), the SSG/LRR-ω model (Eisfeld, 2004; Cécora et al., 2015) and the SSG-ω-Aup model of Aupoix (2012), developed within the European ATAAC project. The SSG/LRR-ω and the SSG-ω-Aup models both use the specific dissipation rate ω as the length-scale providing quantity, due to its improved performance in adverse-pressure-gradient (APG) flow, and thus in aeronautical applications. This behavior, observed for the two-equation $k-\omega$ models, has been explained by Huang and Bradshaw (1995) and Catris and Aupoix (2000) by the mathematical ability of the ω-equation to preserve the log-law prediction in APG, compared to the ε-equation. The SSG-ω-Aup model also uses a specific near-wall approach to correctly reproduce the asymptotic behavior of the turbulent quantities at the wall, including the near-wall model of Manceau and Hanjalić (2002) developed for the EB-RSM.

The SSG/LRR-ω model has already proved to be relevant for industrial cases (Togiti et al., 2014) and has become a trusted base-model for further improvements regarding performance (Togiti and Eisfeld, 2015) and complex flow predictions (Knopp et al., 2018). Although it is generally compared to EVMs (e.g. Eisfeld et al., 2016), especially the $k-\omega$ SST model (Menter, 1994) due to their similarities, it has also been assessed alongside the low-Reynolds-number RSM of Jakirlić and Hanjalić (Cécora et al., 2015; Morsbach et al., 2015). However, the SSG-ω-Aup RSM comes closer to a near-wall version of the SSG/LRR-ω model and appears therefore more appropriate to investigate the benefit of near-wall modeling. Alternatively, the EB-RSM offers a robust near-wall modeling due to its elliptic blending.

All three RSMs have been implemented in a single CFD code, allowing for a systematic and detailed model comparison without influences by the numerical method. They are investigated alongside the Spalart-Allmaras model, a widely applied EVM in the aeronautical industry, on cases of industrial interests, including the Common Research Model (CRM) used in the AIAA Drag Prediction Workshop (Tinoco et al., 2018).

2. Reynolds-stress models

2.1. General formulation

For compressible flow, the Reynolds-averaged Navier-Stokes equations are written using both the Reynolds decomposition $f = \overline{f} + f'$ and the density-weighted average decomposition $f = \widetilde{f} + f''$, where $\widetilde{f} = \overline{\rho f}/\overline{\rho}$,

$$\frac{\partial \overline{\rho}}{\partial t} + \frac{\partial \overline{\rho}\widetilde{U}_i}{\partial x_i} = 0 \tag{1}$$

$$\frac{\partial \overline{\rho}\widetilde{U}_i}{\partial t} + \frac{\partial \overline{\rho}\widetilde{U}_j\widetilde{U}_i}{\partial x_j} = -\frac{\partial \overline{P}}{\partial x_i} + \frac{\partial}{\partial x_j}\left(2\mu\overline{S^*_{ij}} - \overline{\rho}R_{ij}\right) \tag{2}$$

*Corresponding author: gustave.sporschill@gmail.com

where $\overline{\rho}R_{ij} = \overline{\rho u_i'' u_j''}$, and $S^*_{ij} = S_{ij} - S_{kk}\delta_{ij}/3$ is the deviatoric part of the strain-rate tensor $S_{ij} = (\partial_j U_i + \partial_i U_j)/2$. The energy equation is not presented in this paper, which focuses on the different approaches for the modeling of the Reynolds-stress tensor R_{ij} and not on the turbulent heat fluxes[1]. The latter are here simply modeled with a Simple Gradient Diffusion Hypothesis.

Second-moment closures solve transport equations for the Reynolds stresses R_{ij} directly, without relying on the Boussinesq hypothesis that assumes a linear relation between Reynolds-stress and strain-rate tensors. Using Morkovin's hypothesis (Morkovin, 1962), the compressibility terms can be neglected, so that the transport equations read

$$\underbrace{\frac{\partial \overline{\rho} R_{ij}}{\partial t} + \frac{\partial \overline{\rho}\widetilde{U}_k R_{ij}}{\partial x_k}}_{\overline{\rho}C_{ij}} = \underbrace{-\overline{\rho}\left(R_{ik}\frac{\partial \widetilde{U}_j}{\partial x_k} + R_{jk}\frac{\partial \widetilde{U}_i}{\partial x_k}\right)}_{\overline{\rho}P_{ij}} + \underbrace{\frac{\partial}{\partial x_k}\left(\overline{\mu}\frac{\partial R_{ij}}{\partial x_k}\right)}_{\overline{\rho}D^\nu_{ij}} + \overline{\rho}D^T_{ij} + \overline{\rho}\phi^*_{ij} - \overline{\rho}\varepsilon_{ij} \quad (3)$$

where C_{ij}, P_{ij}, D^ν_{ij}, D^T_{ij}, ϕ^*_{ij}, and ε_{ij} denote convection, production, viscous diffusion, turbulent transport, velocity pressure-gradient correlation and dissipation, respectively. The terms on the first line are exact as they only depend on the mean flow velocity and the Reynolds stresses, solved by the equation system. On the contrary, the last three terms involve unknown correlations

$$\overline{\rho}D^T_{ij} = -\frac{\partial \overline{\rho u_i'' u_j'' u_k''}}{\partial x_k}, \quad (4)$$

$$\overline{\rho}\phi^*_{ij} = -\left(\overline{u_i''\frac{\partial p'}{\partial x_j}} - \overline{u_j''\frac{\partial p'}{\partial x_i}}\right), \quad (5)$$

$$\overline{\rho}\varepsilon_{ij} = 2\,\mu\,\overline{\frac{\partial u_i''}{\partial x_k}\frac{\partial u_j''}{\partial x_k}}. \quad (6)$$

The next section describes the different models used to close Eq. (3) at second-moment level.

2.2. Considered models

Three RSMs are investigated in this study and are shortly described and compared in this section:

- the elliptic blending Reynolds-stress model (EB-RSM) (Manceau and Hanjalić, 2002; Manceau, 2015)
- the SSG/LRR-ω RSM (Cécora et al., 2015; Eisfeld et al., 2016)
- the SSG-ω-Aup RSM (Aupoix, 2012)

Different formulations of the SSG/LRR-ω RSM have been proposed and are detailed on NASA's Turbulence Modeling Resource website[2], the one considered here is referred to as `SSG/LRR-RSM-w2012-SD`. The SSG-ω-Aup model is detailed in Appendix A.

[1] details on the energy equation closure can be found on the TMR website https://turbmodels.larc.nasa.gov/implementrans.html

[2] https://turbmodels.larc.nasa.gov/rsm-ssglrr.html

2.2.1. Length-scale providing equation

As for two-equation eddy-viscosity models, the Reynolds-stress transport equation set is closed by adding a length-scale providing transport equation.

The EB-RSM model relies on an ε-equation,

$$\overline{\rho}\frac{\mathrm{D}\varepsilon}{\mathrm{D}t} = \frac{\overline{\rho}}{T}\left(C'_{\varepsilon 1}P_k - C_{\varepsilon 2}\varepsilon\right) + \frac{\partial}{\partial x_j}\left(\overline{\mu}\frac{\partial \varepsilon}{\partial x_j}\right) + \overline{\rho}D^T_\varepsilon. \quad (7)$$

where $T = \max\left(k/\varepsilon; C_T\,(\nu/\varepsilon)^{1/2}\right)$ is the local turbulent time scale, bounded by the Kolmogorov time scale to prevent a singularity at the wall, as k vanishes. To correctly reproduce the peak of production of ε in the buffer layer, the production term is amplified in this region by replacing the constant $C_{\varepsilon 1}$ by a variable coefficient $C'_{\varepsilon 1}$. Several formulations have been suggested (see Manceau, 2015) and the following expression has been retained here

$$C'_{\varepsilon 1} = C_{\varepsilon 1}\left(1 + A_1\left(1 - \alpha^3\right)\sqrt{\frac{k}{R_{ij}n_i n_j}}\right). \quad (8)$$

The SSG/LRR-ω and the SSG-ω-Aup models both use the specific dissipation rate $\omega = \varepsilon/(\beta^* k)$. Indeed, they solve the BSL equation, defined by Menter (1994) as a blending of a Wilcox ω-equation in the inner region with the standard ε-equation in the outer region of the boundary layer

$$\overline{\rho}\frac{\mathrm{D}\omega}{\mathrm{D}t} = \gamma\overline{\rho}\frac{\omega}{k}P_k - \beta\overline{\rho}\omega^2 + \frac{\partial}{\partial x_j}\left(\overline{\mu}\frac{\partial \omega}{\partial x_j}\right) + \overline{\rho}D^T_\omega + 2\,(1 - F_1)\,\frac{\overline{\rho}\sigma^{(\varepsilon)}_\omega}{\omega}\frac{\partial k}{\partial x_j}\frac{\partial \omega}{\partial x_j}. \quad (9)$$

The blending is carried out on the coefficients according to $c = F_1\,c^{(\omega)} + (1 - F_1)\,c^{(\varepsilon)}$, where the baseline function F_1 is unity at the wall and zero in the free-stream region (Eq. (A.15)). This is motivated by the good predictions of Menter's $k - \omega$ model in aeronautical applications and in APG flows.

To improve its prediction in the vicinity of the wall, the SSG-ω-Aup model corrects the dissipation rate ε used in the Reynolds-stress transport equations by adding a damping function and a clipping to an asymptotic behavior in its conversion from ω

$$\varepsilon = f_\varepsilon \max\left(0.09\omega k; \left(\frac{k}{k_0^+}\right)^{3/2}\frac{1}{\kappa y}\right), \quad (10)$$

$$f_\varepsilon = \frac{5}{18} + \frac{13}{18}\tanh\left(\left[\frac{y}{42}\left(\frac{\omega k}{\nu^3}\right)^{1/4}\right]^3\right), \quad (11)$$

where y corresponds to the wall distance. The clipping corresponds to a Yap-type correction to prevent the deviation of the log-law slope in APG flows (see for instance Catris and Aupoix, 2000), whereas the damping function ensures the correct asymptotic behavior of k close to the wall.

2.2.2. Turbulent transport

The EB-RSM uses the Generalized Gradient Diffusion Hypothesis (GGDH) to account for the anisotropy of the turbulent

transport in the boundary layer

$$D_{ij}^T = \frac{\partial}{\partial x_l}\left(C_s\, T\, R_{lm}\frac{\partial R_{ij}}{\partial x_m}\right), \tag{12}$$

$$D_{\varepsilon}^T = \frac{\partial}{\partial x_l}\left(\frac{C_s}{\sigma_\varepsilon}\, T\, R_{lm}\frac{\partial \varepsilon}{\partial x_m}\right), \tag{13}$$

whereas the ω-based RSMs are implemented with the Simple Gradient Diffusion Hypothesis (SGDH)

$$D_{ij}^T = \frac{\partial}{\partial x_l}\left(\frac{2}{3}\frac{C_s}{\beta^*}\nu_t\frac{\partial R_{ij}}{\partial x_l}\right), \tag{14}$$

$$D_{\omega}^T = \frac{\partial}{\partial x_l}\left(\sigma_w \nu_t\frac{\partial \omega}{\partial x_l}\right), \tag{15}$$

with $\nu_t = k/\omega$. It corresponds to the turbulent transport model used in eddy-viscosity models, with an isotropic diffusion coefficient. Although the SSG/LLR-ω RSM is usually defined with the GGDH, it has been considered here with the SGDH to insure a robust model. In the case of the SSG-ω-Aup model, the eddy viscosity used in D_{ij}^T is damped in the near-wall region to account for the wall-blocking effect and bounded as for ε above, see Eq. (A.4) in appendix.

2.2.3. *Velocity pressure-gradient correlation*

The velocity pressure-gradient correlation ϕ_{ij}^* is a critical term to model in second-moment closures. It can be decomposed into a traceless term ϕ_{ij} and a pressure diffusion D_{ij}^p, the traceless term representing a redistribution of the turbulent kinetic energy among the Reynolds stresses. The pressure diffusion is generally assumed to globally contribute to turbulent diffusion, such that D_{ij}^p and D_{ij}^T are modeled as a whole.

The RSMs here use the high-Reynolds-number model proposed by Speziale, Sarkar and Gatski (SSG) (Speziale et al., 1991) for the redistribution far from the wall. It is expressed by

$$\begin{aligned}\phi_{ij} = &-\left(C_1\varepsilon + C_1^* P_k\right) b_{ij}\\ &+ C_2\varepsilon\left(b_{il}b_{jl} - \frac{1}{3}b_{mn}b_{mn}\delta_{ij}\right)\\ &+ \left(C_3 - C_3^*\sqrt{b_{mn}b_{mn}}\right) kS_{ij}^*\\ &+ C_4 k\left(b_{il}S_{jl} + b_{jl}S_{il} - \frac{2}{3}b_{mn}S_{mn}\delta_{ij}\right)\\ &+ C_5 k\left(b_{il}\Omega_{jl} + b_{jl}\Omega_{il}\right).\end{aligned} \tag{16}$$

The constant are given in Table 1. In the EB-RSM, the nonlinear return C_2 term is suppressed to prevent numerical stiffness.

The SSG-ω-Aup model also uses the SSG model, including the C_2 term. However, as the SSG model has been calibrated alongside an ε-equation, the coefficients of the BSL ω-equation are slightly recalibrated to improve the model behavior where the ω-equation is solved (see Appendix A). Both the EB-RSM and the SSG-ω-Aup model rely on a specific near-wall model, presented in Sec. 2.2.5, that activates close to the wall.

In the SSG/LRR-ω RSM, the redistribution term is modeled with a blending of both the SSG and the LRR (Launder et al., 1975) models. Indeed, Wilcox (2006) showed that the ω-equation provides a better behavior in association with the LRR model. The SSG/LRR-ω model thus switches from the SSG model in the free-stream region to the LRR model close to the wall when the BSL equation switches from the ε to the ω-equation. Since both redistribution models can be cast into the same mathematical expression, Eq. (16), the blending is simply applied on their coefficients, similarly to the BSL ω-equation,

$$C = F_1\, C^{(\omega)} + (1 - F_1)\, C^{(\varepsilon)} \tag{17}$$

where F_1 is the baseline function defined in Menter's model (Menter, 1994).

Table 1: Constants for ϕ_{ij} models ($c_2^{\mathrm{LRR}} = 0.52$)

	C_1	C_1^*	C_2	C_3	C_3^*	C_4	C_5
SSG	3.4	1.8	4.2	0.8	1.3	1.25	0.4
LRR	3.6	0	0	0.8	0	$\frac{18c_2^{\mathrm{LRR}}+12}{11}$	$\frac{-14c_2^{\mathrm{LRR}}+20}{11}$

2.2.4. *Dissipation rate*

Considering the deviatoric contribution of ε_{ij} modeled as part of the SSG and the LRR models, the presented RSMs reduce the dissipation rate tensor to its isotropic part

$$\varepsilon_{ij} = \frac{2}{3}\varepsilon\delta_{ij} \tag{18}$$

However, this assumption is no longer valid in the vicinity of the wall, where the flow is strongly anisotropic. As for the redistribution term, the EB-RSM and the SSG-ω-Aup model therefore rely on a specific near-wall model.

2.2.5. *Near-wall modeling*

The presence of a solid wall implies an amplified damping of the wall-normal Reynolds stress R_{22} due to the blocking effect of the wall, asymptotically leading to a two-component turbulence. The Taylor-series expansion of the Reynolds stresses yields

$$R_{11} \sim y^2, \qquad R_{22} \sim y^4, \qquad R_{33} \sim y^2. \tag{19}$$

To reproduce this physical phenomenon, the EB-RSM and the SSG-ω-Aup model use a specific near-wall modeling for ε_{ij} and ϕ_{ij} ensuring the correct asymptotic behavior. They both rely on Rotta's near-wall dissipation model ε_{ij}^w (Rotta, 1951) and Manceau & Hanjalić asymptotic redistribution model ϕ_{ij}^w (Manceau and Hanjalić, 2002)

$$\varepsilon_{ij} = (1 - f_b)\,\varepsilon_{ij}^w + f_b\,\frac{2}{3}\varepsilon\delta_{ij}, \qquad \varepsilon_{ij}^w = \frac{R_{ij}}{k}\varepsilon, \tag{20}$$

$$\begin{aligned}\phi_{ij} &= (1 - f_b)\,\phi_{ij}^w + f_b\,\phi_{ij}^{SSG},\\ \phi_{ij}^w &= -5\frac{\varepsilon}{k}\left(R_{ik}n_jn_k + R_{jk}n_in_k - \frac{1}{2}R_{kl}n_kn_l\left(n_in_j + \delta_{ij}\right)\right).\end{aligned} \tag{21}$$

Table 2: Differences between the considered models in the near-wall region

	EB-RSM	SSG-ω-Aup RSM	SSG/LRR-ω RSM
Length-scale	ε	ω BSL (recalibrated) near-wall corrected ε	ω BSL $\varepsilon = \beta^* \omega k$
ε_{ij} at the wall	Rotta, Eq. (20)	Rotta, Eq. (20)	isotropic
ϕ_{ij} at the wall	Manceau & Hanjalić, Eq. (21)	Manceau & Hanjalić, Eq. (21)	LRR
D_{ij}^T	GGDH	SGDH	SGDH
f_b	elliptic blending	analytic blending	BSL function F_1

However, these two models differ in their blending functions f_b. The SSG-ω-Aup model uses an analytic function, depending on the wall-distance y

$$f_b = 1 - \exp\left(-\left[\frac{1}{225}\left(\frac{\omega y^2}{\nu} - \frac{6}{\beta}\right)\right]^2\right), \tag{22}$$

with $\beta = 3/40$. It can be noted that the terms in the innermost parentheses correspond to the asymptotic solution of the ω-equation close to the wall, so that $f_b = 0$ at the wall.

On the other hand, the EB-RSM is based on the elliptic blending to avoid any direct dependence on the wall-distance. As a simplification of Durbin's elliptic relaxation (Durbin, 1991) down to only one additional equation, the elliptic blending (Manceau and Hanjalić, 2002) let the EB-RSM sense the distance to the wall from a characteristic local length scale L to adapt the transition between near-wall and free-stream modeling

$$\alpha_{EB} - L^2 \nabla^2 \alpha_{EB} = 1, \tag{23}$$

$$L = C_L \max\left(\frac{k^{3/2}}{\varepsilon}; C_\eta \left(\frac{\nu^3}{\varepsilon}\right)^{1/4}\right). \tag{24}$$

For an optimal behavior, the blending function is set to $f_b = \alpha_{EB}^3$ (Manceau, 2015).

2.2.6. *Summary*

In the free-stream region, all three RSMs behave similarly. Indeed, they all rely on the SSG model for the velocity pressure-gradient modeling, with an isotropic dissipation and the use of an ε-equation to transport the dissipation rate.

However, they differ in their near-wall modeling. Both the SSG/LRR-ω model and the SSG-ω-Aup model switch to a ω-equation, but the SSG-ω-Aup model uses a specific relation for the ω-to-ε conversion to ensure a correct behavior in the vicinity of the wall. While the SSG/LRR-ω model switches ϕ_{ij}^* models only out of reason of compatibility with the BSL ω-equation, the others ensure a correct asymptotic behavior for ε_{ij} and ϕ_{ij}^* by using a specific asymptotic near-wall model. Finally, all models have their own blending functions to activate their near-wall modeling. Table 2 sums up the near-wall differences.

These models have been implemented at Dassault Aviation in the in-house CFD code Aether (Chalot, 2004). It is an unstructured continuous finite element solver for the compressible Navier-Stokes equations, stabilized using the Streamline Upwind Petrov-Galerkin (SUPG) method. Aether is written using the entropy formulation Mallet (1985), which offers many advantages, in particular symmetric operators with positivity properties and efficient preconditioning. Continuity, momentum, energy as well as turbulence equations are solved using linear spatial interpolation functions, yielding a 2$^{\text{nd}}$-order spatial scheme. Turbulence convective terms are addressed with N-scheme. A steady state algorithm is used to approach the converged solution, using local time stepping. The local CFL number is dynamically updated according to the convergence quality and a maximum CFL value of 50 is allowed. The linear systems are solved using preconditioned GMRES method. Navier-Stokes and turbulence equations are solved in a decoupled manner. Finally, realisability constraints, positive diagonal stress and Cauchy-Schwartz inequality, are enforced for the Reynolds stresses. The calculations are considered converged when the residuals of the Navier-Stokes equations have decreased by at least 5 orders of magnitude and the aerodynamic forces have reached a plateau.

3. Zero-pressure-gradient boundary layer

The models are first assessed in the case of a flat plate, zero-pressure-gradient boundary layer to analyze the fundamental differences between the Reynolds-stress models implemented. The computations are run for a Mach number of $M_\infty = 0.2$ and $Re = 5\,\text{M}$. A uniform velocity profile is imposed at the inlet, upstream of the leading edge. The mesh convergence study has been carried out using the different meshes provided by NASA[3], whose characteristics are gathered in Table 3.

Table 3: Meshes characteristics

Mesh	Resolution	Total nodes
M1	35×25	875
M2	69×49	3,381
M3	137×97	13,289
M4	273×193	52,689
M5	545×385	209,825

[3] https://turbmodels.larc.nasa.gov/flatplate_grids.html

Figure 1 shows the friction coefficient predicted by the models for the different meshes. Note that the convergence is assessed at a given $Re_\theta = U_\infty \theta/\nu$ rather than at a fixed position, as proposed by NASA. The comparison position is thus defined with respect to the predicted boundary layer rather than to the flat plate geometry. Hence, the boundary layer growth rates on the different refined meshes are accounted for.

It can be seen from the figure that the third mesh offers a satisfactory refinement for all the models. Unlike the EB-RSM and the SSG/LRR-ω RSM, the SSG-ω-Aup model already yields a good estimate of the skin friction on the coarsest mesh, with a maximum relative error of 0.8 % for the mesh M2. The resolution needed to properly converge the different RSMs appears similar to the one needed for Spalart-Allmaras model. In the following, the four models are compared on mesh M3.

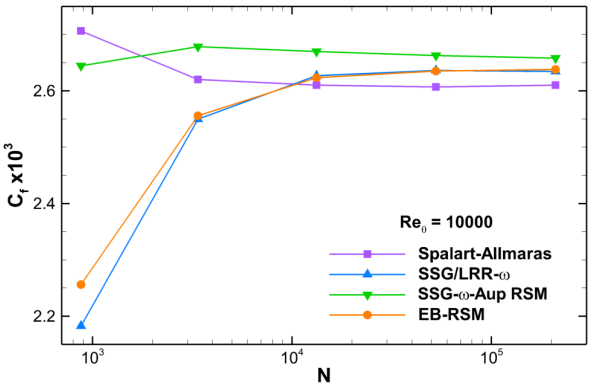

Figure 1: Mesh convergence for the flat plate at $Re_\theta = 10{,}000$

The results are assessed using empirical correlations, the DNS data of Schlatter et al. (2010) and the results given by the Spalart-Allmaras model used as a reference.

3.1. Integral quantities

The evolution of the integral quantities in the boundary layer is compared with empirical laws. Using the von Kármán integral equation without pressure gradient, $\mathrm{d}\theta/\mathrm{d}x = C_f/2$, with an experimentally calibrated $1/7^{\text{th}}$-power-law velocity profile (Schlichting, 1979), the displacement and the momentum thicknesses are expressed as

$$\delta^* = \int_0^\infty \left(1 - \frac{U}{U_\infty}\right) \mathrm{d}y \approx \frac{0.048x}{Re_x^{1/5}}, \tag{25}$$

$$\theta = \int_0^\infty \frac{U}{U_\infty}\left(1 - \frac{U}{U_\infty}\right) \mathrm{d}y \approx \frac{0.037x}{Re_x^{1/5}}, \tag{26}$$

and are valid for $Re_x < 10^7$ for a boundary layer turbulent from the leading edge.

Fig. 2 shows the good agreement of the Reynolds-stress models with these empirical laws. In particular, the ω-based RSMs satisfactorily predicts δ^*, whereas the EB-RSM slightly overpredicts it towards the end of the domain. Regarding the momentum thickness, the RSMs seem to better predict θ compared to the Spalart-Allmaras model, which slightly underpredicts the

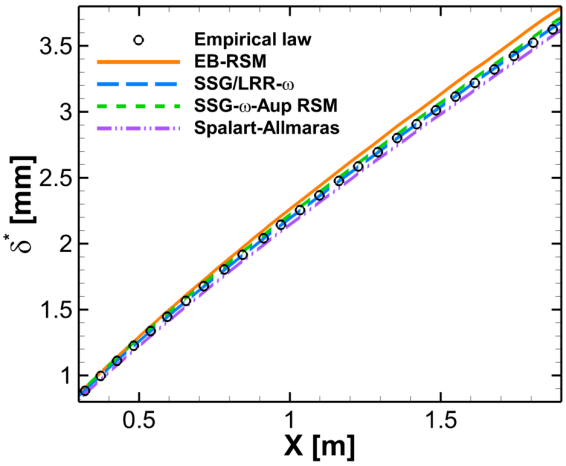

(a) Displacement thickness

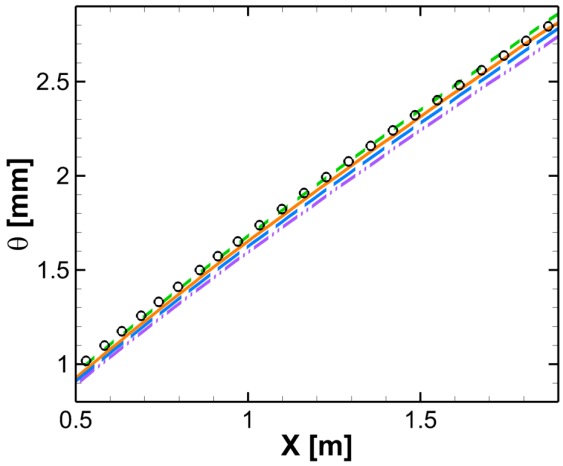

(b) Momentum thickness

Figure 2: Boundary layer thicknesses on the flat plate

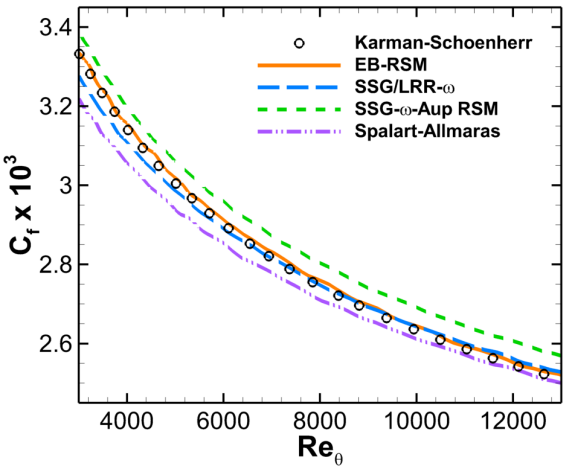

Figure 3: Skin friction coefficient on the flat plate

integral thicknesses. Here, the SSG/LRR-ω model still underpredicts θ by about 2.5 %.

The local skin friction is shown in Fig. 3. The models are benchmarked against the Kármán-Schoenherr relation (Schoenherr, 1932)

$$C_f = \frac{1}{17.08\,(\log_{10} Re_\theta)^2 + 25.11 \log_{10} Re_\theta + 6.012}, \tag{27}$$

for 4,000 < Re_θ < 13,000 as suggested by NASA.

Both the EB-RSM and the SSG/LRR-ω model improve the predictions over the Spalart-Allmaras model on a large range of Reynolds numbers. In Fig. 3, they closely follow the empirical relation. The Spalart-Allmaras model recovers to the target skin friction at the highest Re_θ, reducing the relative error from 2.8 % at Re_θ = 4,000 down to 0.4 % at Re_θ = 12,000. Despite a correct trend over the entire flat plate, the SSG-ω-Aup model systematically overestimates the skin friction of about 2 %.

3.2. *Profiles at Re_θ = 4060*

The results are compared with the flat plate DNS of Schlatter et al. (2010). The profiles are extracted at the same Reynolds numbers Re_θ as in the DNS.

Fig. 4 shows the profiles in wall-units for Re_θ = 4,060, the highest Reynolds number available in the reference. As expected, the mean velocity profile is correctly predicted by all the models in Fig. 4(a). It can be noted though that the SSG-ω-Aup model underestimates the velocity in the wake region, whereas the EB-RSM and the SSG/LRR-ω model tend to underestimate the buffer layer velocity. These observations are confirmed by the turbulent shear-stress, which directly affects the mean velocity. Fig. 4(b) indeed shows good overall predictions, but the SSG-ω-Aup model returns to zero in the free-stream region more gradually than the DNS, and the other RSMs amplify the shear-stress in the vicinity of $y^+ \approx 10$ by 10 % with a slightly steeper gradient. The stronger shear-stress in these regions increases the mixing between the low-momentum fluid closer to the wall and the higher-momentum fluid further away, resulting in an underestimation of the mean velocity where $|R_{12}|$ is too large compared to the DNS.

Figs. 4(c)–(e) highlight the difference in the modeling approaches. Both the EB-RSM and the SSG-ω-Aup model correctly reproduce the two-component turbulence at the wall by means of the near-wall model Eq. (21) of Manceau and Hanjalić (2002), with R_{11} and R_{33} decreasing in y^2 whereas R_{22} decreases in y^4. They also predict the peaks in the buffer layer for R_{11} and R_{33}. This can be related to the ε-equation in the EB-RSM and the improved ω-to-ε conversion Eq. (10) of the SSG-ω-Aup model, whose effectiveness is evidenced here by the fact that it yields a non-zero constant dissipation rate in the viscous sublayer, as shown in Fig. 4(f).

This behavior is to be compared to the vanishing dissipation rate with the SSG/LRR-ω model and its exaggerated peak in the buffer layer. Indeed, without the corrected conversion, the SSG/LRR-ω model is unable to reproduce any peak for R_{11} and R_{33}. Moreover, due to the lack of near-wall modeling, the model fail to predict the two-component turbulence at the wall, with all the Reynolds stresses decreasing in y^3.

3.3. *Turbulence budgets*

The models can be further analyzed by looking at the budget of the Reynolds stresses. Figs. 5 & 6 compares the different source terms of the transport equations for R_{11} and R_{22}.

The vanishing of ε at the wall for the SSG/LRR-ω model shown in Fig. 4(f) results in the component ε_{11} of the dissipation tensor to tend to zero as well in Fig. 5(b). Since the dissipation term balances the viscous diffusion at the wall, the fact that it tends to zero with this model is at the origin of the cancellation of viscous diffusion D^ν_{11}. As a consequence, since its secondary derivative is zero, R_{11} behaves as y^3 in the vicinity of the wall as mentioned above.

The near-wall modeling in the EB-RSM and the SSG-ω-Aup model improves this behavior. In particular, the blending of the SSG model with the near-wall model Eq. (21) of Manceau and Hanjalić (2002) corrects the amplitude of their redistribution terms ϕ^*_{11} and ϕ^*_{22}. The near-wall modeling also damps the source terms for R_{22} in the viscous sublayer and in the buffer layer, so that the wall-normal stress correctly decreases as $\propto y^4$ at the wall.

Figs. 5(d) & 6(d) highlight the differences between the GGDH model used in the EB-RSM and the SGDH in the other RSMs. In particular, the SGDH overpredicts the peaks of turbulent transport in the buffer layer. Despite an improved amplitude, the GGDH does not correctly predict the negative diffusion of R_{22} for $y^+ \approx 30$.

To analyze the relative amplitude of the different terms as they vanish, Fig. 7 presents the budgets in a proportional way, as proposed by Billard (2012). The terms are decomposed into their positive and negative contributions, so that the transport equation can be written

$$\frac{\partial R_{ij}}{\partial t} = \sum_k T_k^+ + \sum_k T_k^-, \tag{28}$$

with $T_k^+ = \max(T_k, 0)$, $T_k^- = \min(T_k, 0)$.

The flow considered is stationary, thus $\partial_t R_{ij} = 0$ and the balance of the transport equation imposes $\sum_k T_k^+ = -\sum_k T_k^-$. The terms are then rescaled according to the budget amplitude $\sum_k T_k^+$ at each point of the boundary layer to indicate the proportion of each term at a given distance to the wall.

Using a DNS, this presentation enables to gain understanding of the physical phenomena at play. It also illustrates the ability of the Reynolds-stress models to reproduce these phenomena. Fig. 7 especially highlights the main regions of the boundary layer.

The logarithmic layer corresponds to the range where the molecular diffusion D^ν_{ij} vanishes and the convection C_{ij} is not yet involved. For infinite Reynolds numbers, turbulent transport is also expected to vanish, which is not entirely the case in the considered DNS with Re_θ = 4,060. One third of the production of R_{11} is dissipated, whereas the rest is redistributed to the other stresses. In particular, this redistribution feeds R_{22} and is almost

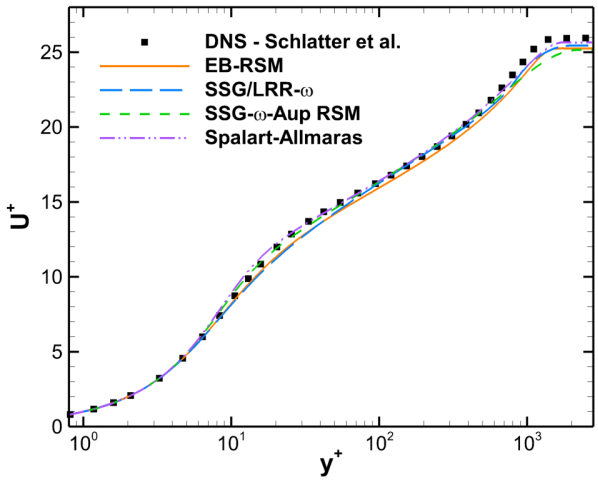

(a) Mean velocity

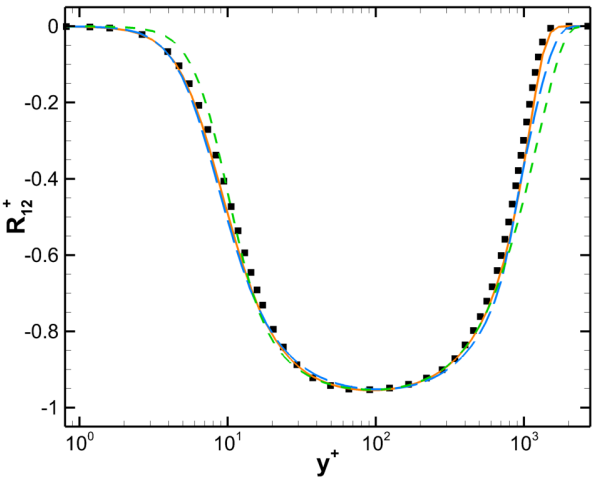

(b) Turbulent shear-stress

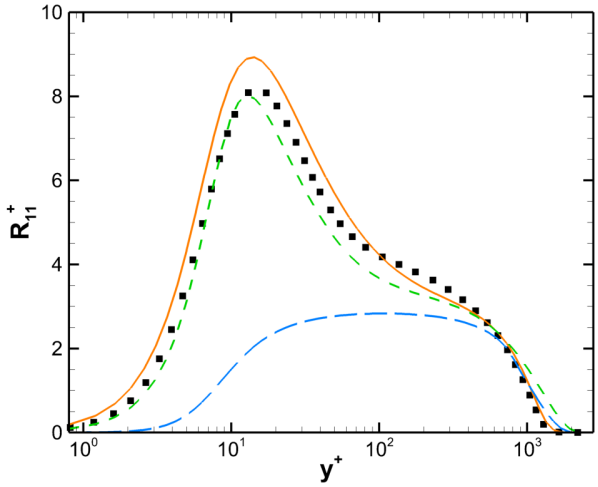

(c) Streamwise Reynolds stress

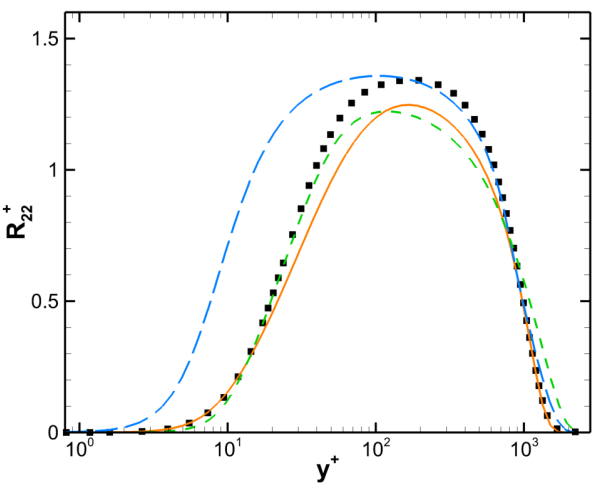

(d) Wall-normal Reynolds stress

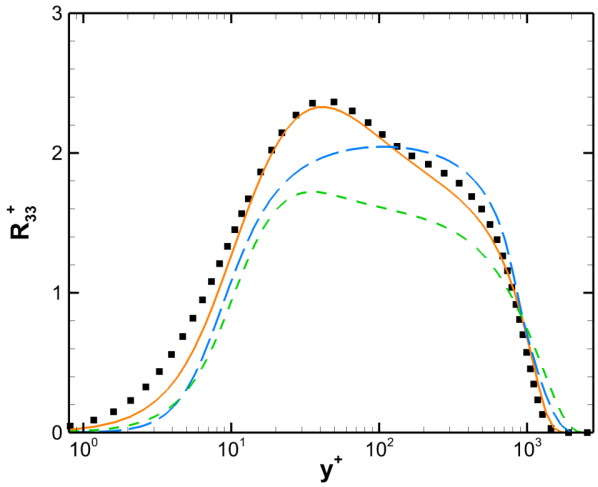

(e) Spanwise Reynolds stress

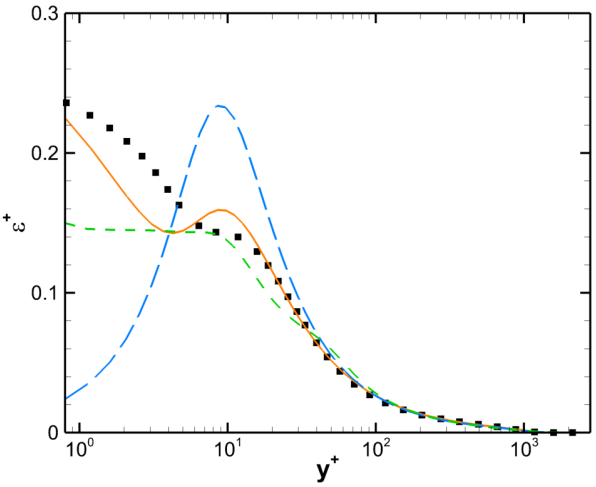

(f) Dissipation rate

Figure 4: Profiles on the flat plate at Re_θ = 4,060

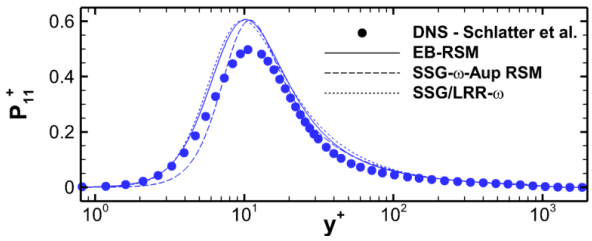

(a) Production of R_{11}

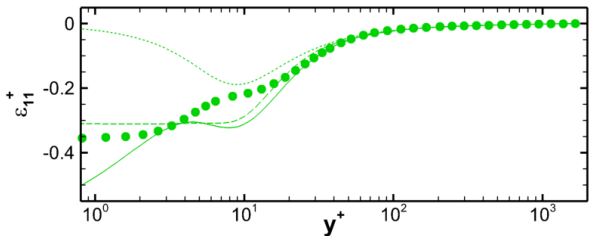

(b) Dissipation of R_{11}

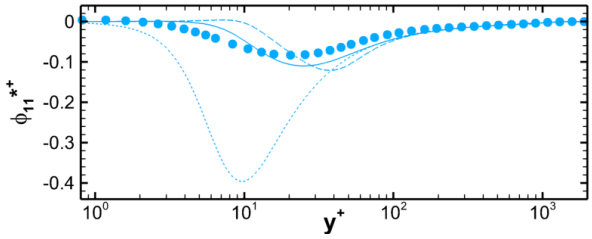

(c) Redistribution of R_{11}

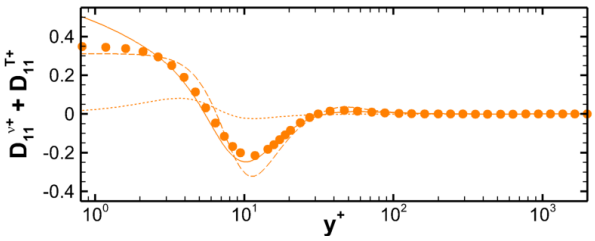

(d) Total diffusion of R_{11}

Figure 5: Reynolds-stress source terms of R_{11} on the flat plate at $Re_\theta = 4{,}060$

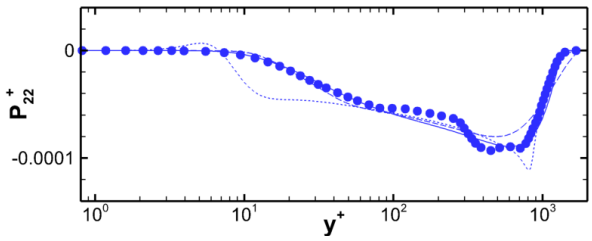

(a) Production of R_{22}

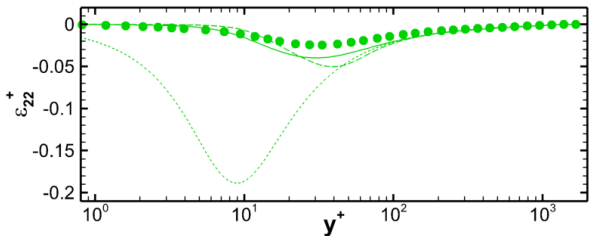

(b) Dissipation of R_{22}

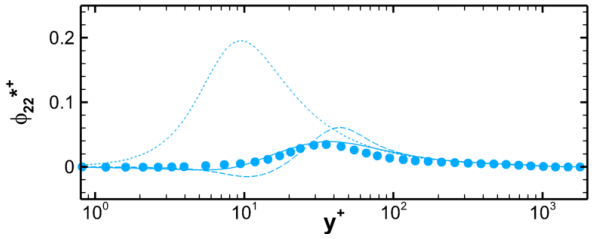

(c) Redistribution of R_{22}

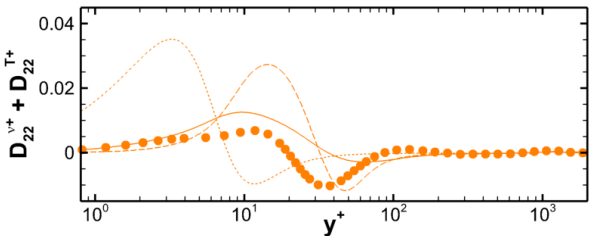

(d) Total diffusion of R_{22}

Figure 6: Reynolds-stress source terms of R_{22} on the flat plate at $Re_\theta = 4{,}060$

entirely dissipated in the log layer. This behavior is well reproduced by all models. Similarly, the models correctly predict the balance between turbulent transport and convection in the outer region, as observed in the DNS, Figs. 7(a) & (b).

The main discrepancies appear as expected in the near-wall region. The viscous sublayer in the SSG/LRR-ω displays an erroneous redistribution: ϕ^*_{11} is taking energy from R_{11} at the wall to feed R_{22}, in the continuation of the log layer behavior for which the LRR model has been calibrated. Consequently, ϕ^*_{22} does not reproduces the wall-blockage effect, which leads to redistribute the energy of the wall-normal stress towards all others stresses.

This phenomenon is on the contrary visible for the EB-RSM (d) and the SSG-ω-Aup model (f). The relative contributions of ϕ^*_{22} and ε_{22} is however different from the $^2/_5 - {}^3/_5$ distribution in the DNS. As explained in Manceau and Hanjalić (2002), the near-wall model aims at correctly predicting the difference $\phi^*_{22} - \varepsilon_{22}$ at the wall, which is involved in the budget, rather than each term individually, and compensates especially for the asymptotic shortcomings of Rotta's near-wall dissipation Eq. (20) (Rotta, 1951). For these two models, the spatial extent of the negative ϕ^*_{22} is larger than what is observed for the DNS (b). This region extended towards the buffer layer balances the turbulent transport D^T_{22} and is all the larger for the SSG-ω-Aup model as the SGDH exaggerates the turbulent transport D^T_{22} in the buffer layer, as observed in Fig. 6(d).

A non-zero residual can be observed with the models, especially with the EB-RSM, for $y^+ > 10^3$, corresponding to the free-stream region. In this region, the turbulence tends to vanish so that the dependent turbulent variables, ε in the EB-RSM and ω in the other models, are bounded to prevent numerical stiffness, hence the presence of a small residual.

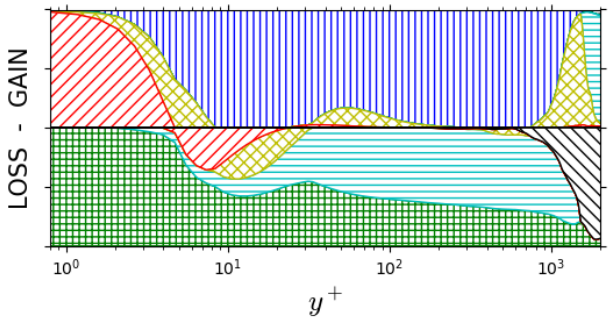

(a) Budget of R_{11}, DNS – Schlatter *et al.* (Schlatter et al., 2010)

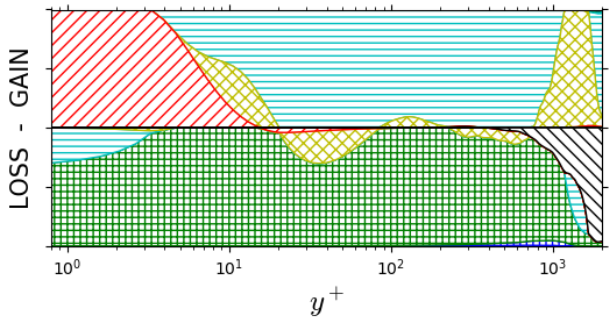

(b) Budget of R_{22}, DNS – Schlatter *et al.* (Schlatter et al., 2010)

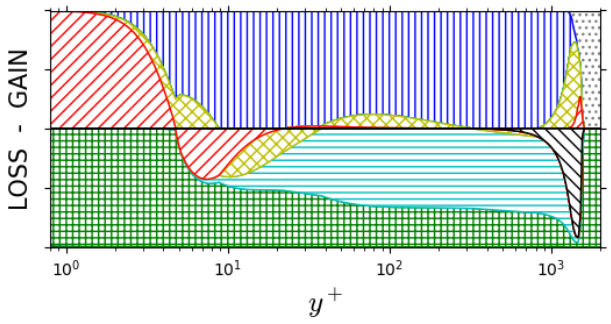

(c) Budget of R_{11}, EB-RSM

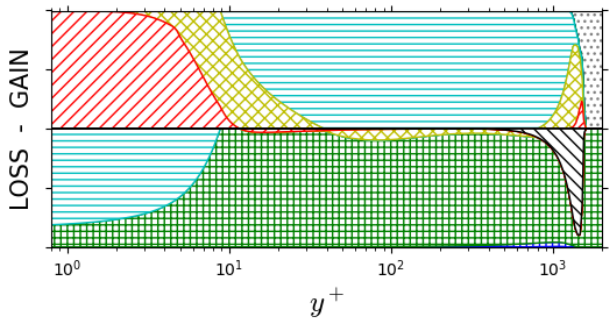

(d) Budget of R_{22}, EB-RSM

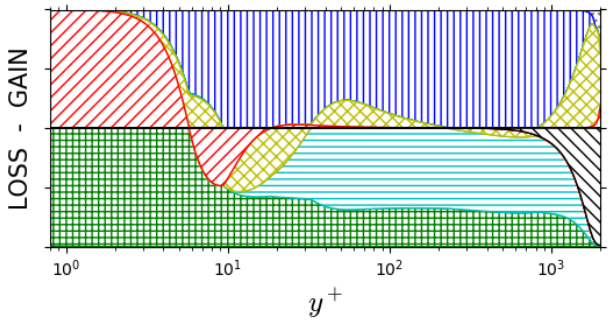

(e) Budget of R_{11}, SSG-ω-Aup RSM

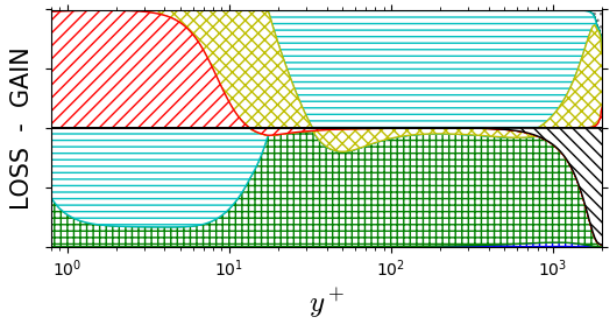

(f) Budget of R_{22}, SSG-ω-Aup RSM

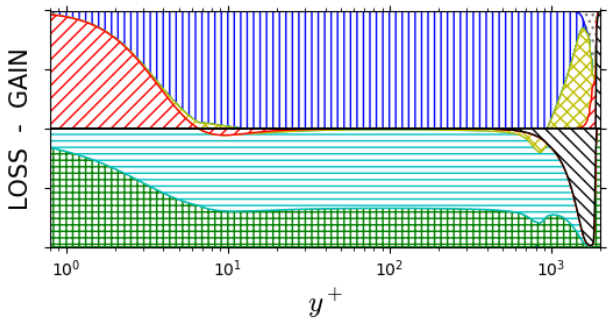

(g) Budget of R_{11}, SSG/LRR-ω

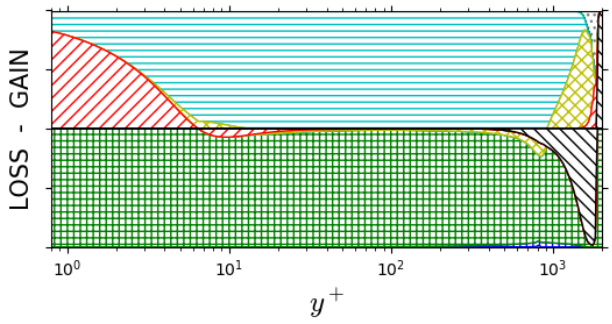

(h) Budget of R_{22}, SSG/LRR-ω

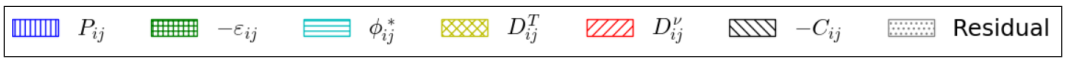

Figure 7: Proportional budgets on the flat plate at Re_θ = 4,060

This section highlighted the difference between Reynolds-stress models enforcing the correct near-wall stress behavior through an asymptotic approach, and the SSG/LRR-ω model, which does not. The near-wall modeling greatly improves the Reynolds-stress profiles, and especially helps the models to reproduce the physical features of turbulence at the wall, such as the two-component limit and the peaks in the buffer layer. However, the lack of this specific modeling does not prevent the SSG/LRR-ω RSM to yield satisfactory results regarding the mean flow, close to the other RSMs.

4. Application cases

4.1. Adverse-pressure-gradient boundary layer

The Skåre & Krogstad wind-tunnel experiment (Skåre and Krogstad, 1994) aimed at gathering data on an adverse-pressure-gradient (APG) turbulent boundary layer at equilibrium. The setup, shown in Fig. 8, consists in a diverging wind-tunnel with a 6 m long test section, which upper-wall profile $h(x)$ was adjusted to let the lower boundary layer reach an equilibrium state under APG, defined as a region where the velocity profiles are self-similar. The streamwise evolution of the boundary layer becomes independent of the flow history, thus simplifying the study of the impact of the pressure-gradient on the flow. The equilibrium is characterized by a constant pressure-gradient parameter β_p introduced by Clauser (1954)

$$\beta_p = \frac{\delta^*}{\tau_w}\frac{\mathrm{d}P_w}{\mathrm{d}x}. \tag{29}$$

The equilibrium region is achieved for $4.0\,\mathrm{m} \leqslant x \leqslant 5.0\,\mathrm{m}$, with $Re_\theta \in [39{,}000\,;\,51{,}000]$ and $\beta_p = 20$. This experiment is a case relevant to the aeronautical industry as it is representative of the strong pressure gradients and high Reynolds numbers found at the trailing edge of wings, as shown for instance in Fig. 9 for NASA's Common Research Model.

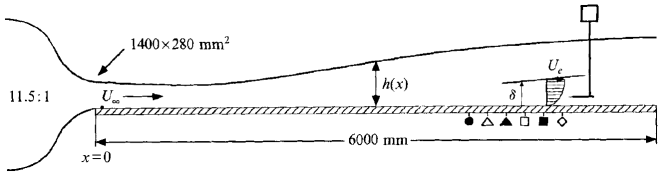

Figure 8: Skåre & Krogstad experiment configuration (reproduced from Skåre and Krogstad (1994))

The numerical simulations have been carried out on the 3D geometry of the wind-tunnel, to account for the non-negligible three-dimensional effects. For instance, a strong recirculation develops in the upper corner and compresses the flow in the symmetry plan, as shown in Fig. 10 for the Spalart-Allmaras model. This ensures a correct prediction of the pressure coefficient distribution, hence a correct pressure-gradient. Moreover, the geometry is extended with a straight channel up to $x = 9.0\,\mathrm{m}$ with constant pressure outlet. The resulting mesh includes 13 M nodes, with a first-cell height of $y^+ < 0.5$, following the convergence study carried out by Paysant (2016).

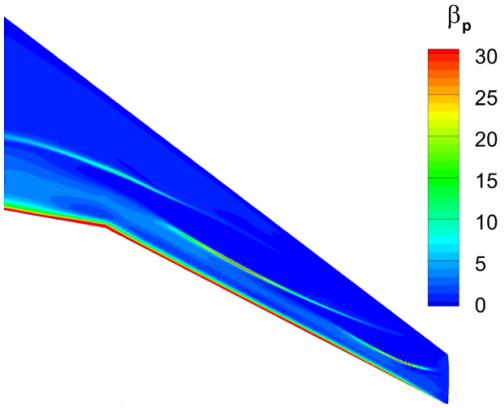

Figure 9: Predicted β_p on the wing of the CRM with the Spalart-Allmaras model ($Re_c = 30\,\mathrm{M}$, $C_L = 0.4$)

The Spalart-Allmaras model is here completed with the Quadratic Constitutive Relation (QCR) (Spalart, 2000), which adds anisotropy to the Boussinesq hypothesis to improve the behavior of the model, especially in corner flows. The SSG-ω-Aup model severely overpredicts the recirculation in the upper corner and fails to converge. Its results on this case will therefore not be presented.

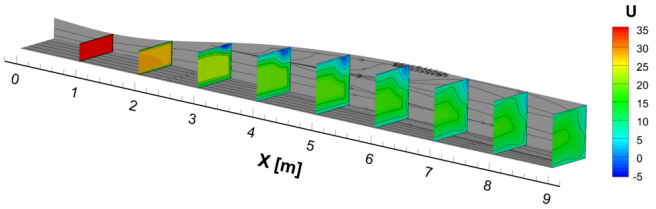

Figure 10: Flow topology for the Spalart-Allmaras QCR model. The lines indicate the skin friction direction.

4.1.1. Integral quantities

The boundary layer quantities are shown in Fig. 11. The experimental equilibrium region is clearly visible in Figs. 11(a)–(b), displaying a constant pressure-gradient parameter β_p within $x \in [4.0\,\mathrm{m}\,;\,5.0\,\mathrm{m}]$.

On the other hand, none of the models achieve the equilibrium flow, according to Fig. 11(b). Instead of a plateau starting from $x = 4.0\,\mathrm{m}$, β_p decreases for all three models after reaching a peak between $x = 3.5\,\mathrm{m}$ and $x = 4.0\,\mathrm{m}$. The β_p-distribution upstream of the peak for the RSMs is consistent with the upstream experimental measurements.

Both RSMs yield good predictions of the skin friction at $x = 3.0\,\mathrm{m}$ but overpredict it downstream, resulting in a relative error to the experiment of 42 % and 67 % at $x = 5.0\,\mathrm{m}$ for the EB-RSM and the SSG/LRR-ω model respectively. The Spalart-Allmaras model here exhibits a better prediction of C_f in the equilibrium region, despite the exaggerated drop in the upstream region, for $x \leqslant 3.0\,\mathrm{m}$.

The discrepancy observed with the pressure-gradient parameter is explained by the deviation of the displacement thickness,

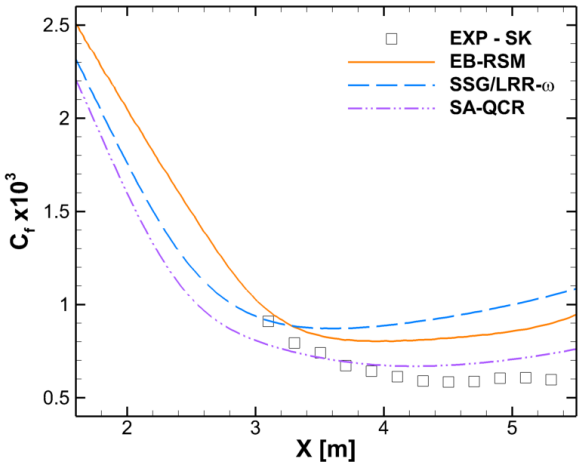

(a) Skin friction coefficient

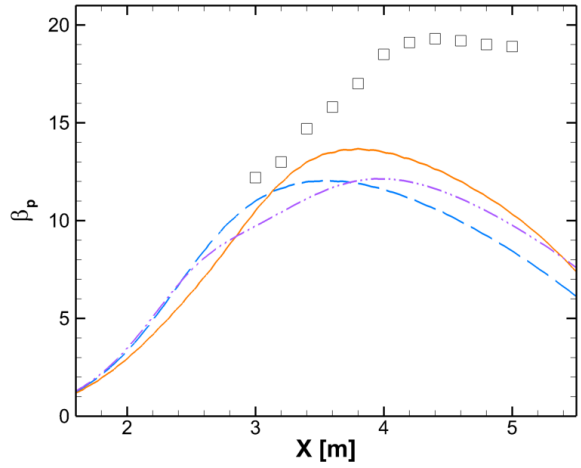

(b) Clauser's pressure-gradient parameter

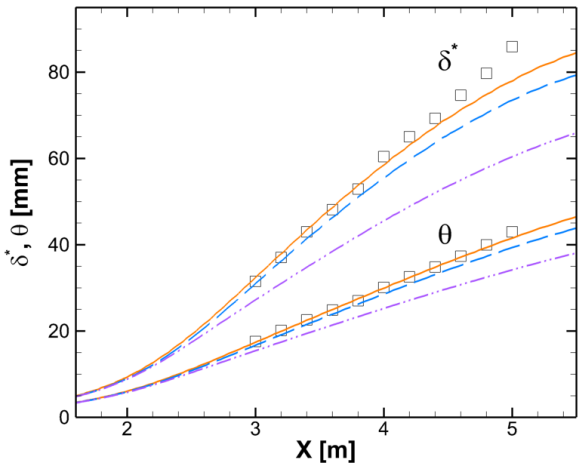

(c) Displacement and momentum thicknesses

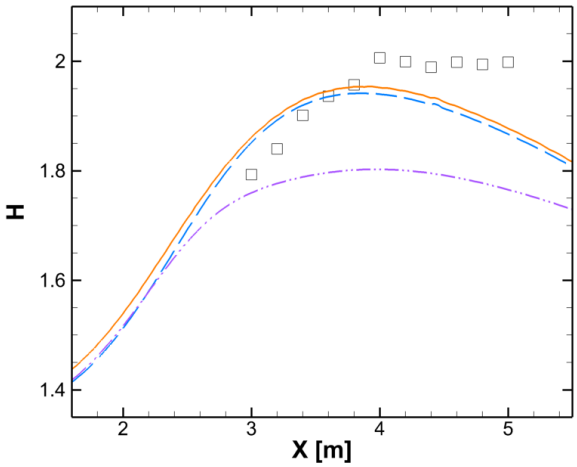

(d) Shape factor

Figure 11: Integral quantities in the instrumented region of the Skåre & Krogstad wind-tunnel

which enters the definition (29) of the parameter. Fig. 11(c) shows indeed that for the RSMs, δ^*, and to a lesser extent θ, progressively deviate from the measurements around the predicted peak of β_p. The figure also highlights the correct growth of their boundary layers upstream, as they reach the experimental values for $x = 3.0\,\mathrm{m}$. In contrast, the Spalart-Allmaras model underpredicts both thicknesses downstream of $x = 3.0\,\mathrm{m}$, which explains the poor prediction of the pressure-gradient parameter despite a C_f prediction closer to the reference.

The underprediction of the boundary layer growth of the Spalart-Allmaras model also results in a less accurate shape factor $H = \delta^*/\theta$, plotted in Fig. 11(d). The RSMs improve the minimum relative error of H to the measurements in the equilibrium region from about 10 % for the Spalart-Allmaras model down to 2.5 %–5 %.

4.1.2. Profiles

Three profiles in the experimental equilibrium region are compared in Fig. 12, for $x \in \{4.2\,\mathrm{m}\,; 4.6\,\mathrm{m}\,; 5.0\,\mathrm{m}\}$.

Fig. 12(a) shows the mean velocity profiles in a linear scale. Both RSMs clearly improve the predictions over the Spalart-Allmaras model, as they fit the experimental data on most of the outer layer, especially the EB-RSM. It can be noted that the SSG/LRR-ω model displays a bump in the outer layer, which can be related to the tendency of the model to smooth the transition between the boundary layer and the free-stream region. This smooth transition can also be noticed on the flat plate (Fig. 4(a)). These remarks are in agreement with the previous section, the RSMs correctly predicting the boundary layer growth compared to the Spalart-Allmaras model, the SSG/LRR-ω model yet underpredicting the thicknesses δ^* and θ. However, both RSMs progressively overpredict the velocity in the inner region ($Y/\delta \leqslant 20\,\%$) with the streamwise position. This reflects

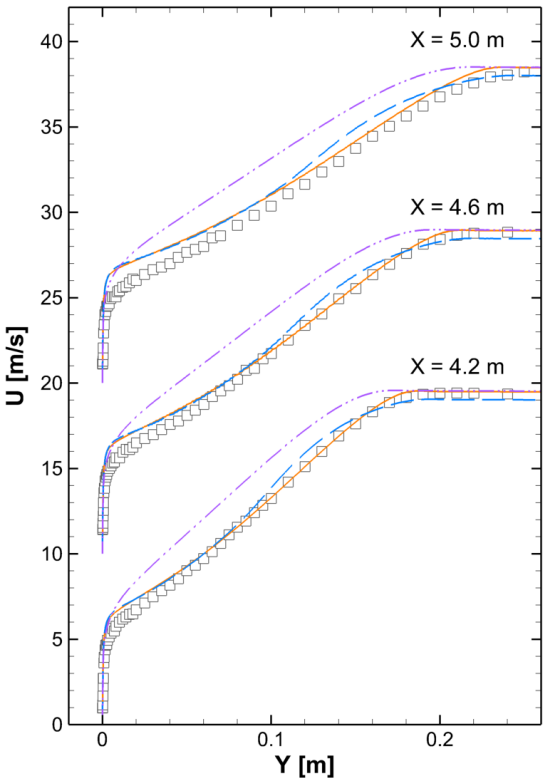

(a) Physical quantities

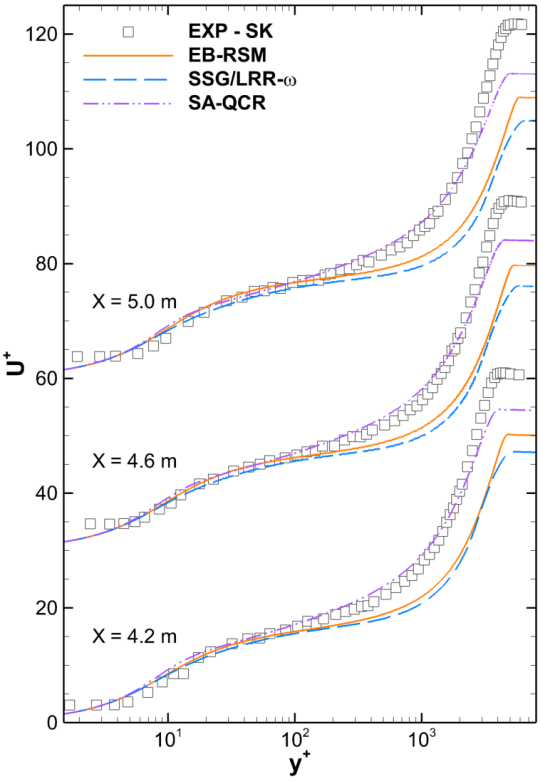

(b) Wall-units

Figure 12: Mean velocity profiles in the equilibrium region for the Skåre & Krogstad wind-tunnel

the inability of these models to correctly slow down the flow in the inner layer, and explains the deviation of the integral quantities, especially H and the skin friction C_f.

Velocity profiles are more often looked at in wall-units, as shown in Fig. 12(b), where the Spalart-Allmaras model appears to behave better. This is an artefact of the scaling with the friction velocity $u_\tau = U_\infty \sqrt{C_f/2}$. Indeed, it has been seen in Fig. 11(a) that the RSMs overpredict the skin friction. Their comparison with the experiments is thus deteriorated by the scaling in wall units, in contrast to what is observed for the Spalart-Allmaras model. Besides, the progressive distortion of the inner layer for the RSMs in Fig. 12(a) seems related to the prediction of a thick and abnormally flat logarithmic layer, with an apparent von Kármán constant of $\kappa \approx 0.60$. This predicted value can be compared to the experimental value measured here at $\kappa = 0.38$, which is consistent with Nickels's analysis of the log law in APG (Nickels, 2004) and recent experiments (Knopp et al., 2021). Further corrections of RSMs in the inner layer yield promising results (Knopp et al., 2018).

4.2. Common Research Model

The Reynolds-stress models are applied to the Common Research Model (CRM), used in the AIAA Drag Prediction Workshop (Vassberg et al., 2008; Tinoco et al., 2018). It represents a generic commercial aircraft and its 'wing-body' configuration is here selected to keep the case simple and more representative of aircraft designed at Dassault Aviation, whose engines are located at the rear of the fuselage.

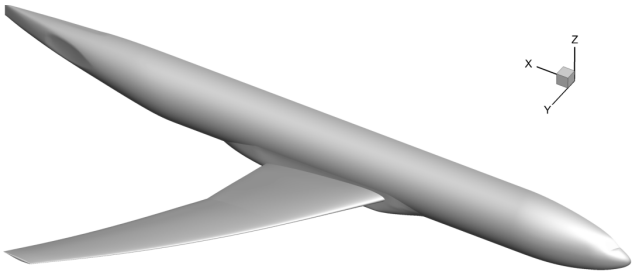

Figure 13: The CRM 'Wing-Body' configuration

The case is run at Mach number $M_\infty = 0.85$ for $Re_c = 5$ M and $Re_c = 30$ M. The turbulence models are compared to wind-tunnel measurements of the NTF (National Transonic Facility), which include wall corrections to account for the wind-tunnel walls in the test section. The geometries used account for the aeroelastic deformation at $C_L = 0.5$ for $Re_c = 5$ M and at $C_L = 0.4$ for $Re_c = 30$ M, using deflection measurements of the ETW (European Transonic Wind-tunnel) facility (Keye and Gammon, 2016). Additionally, the base geometry for $C_L = 0$ is also considered in lift and drag polars to account for the progressive deflection of the aircraft model.

The mesh convergence was confirmed with the Spalart-Allmaras QCR model, by comparison with the results from the workshop participants. This led to meshes with 17.3 M and 20 M nodes for the $Re_c = 5$ M and $Re_c = 30$ M cases respectively, and with a first-cell height of $y^+ < 1$.

4.2.1. Drag polars

To assess the benefits of Reynolds-stress models in aircraft design more generally, the lift and drag predictions have been investigated. Polars have been computed between $C_L = 0.2$ and the nominal lift coefficient of the cases presented above, to analyze the predicted variations of the aerodynamic load on the aircraft during flight. To correctly predict the performance of the designed aircraft geometry and its overall fuel consumption, lift and drag variations must therefore be accurately anticipated, using drag polars. In particular, these polars make it possible here to assess the accuracy of the response in drag to a given lift variation for the considered models.

To account for the aircraft aeroelasticity, computations have been run for each case on both base ($C_L^{\text{shape 1}} = 0$) and deformed geometries of the CRM, with $C_L^{\text{shape 2}} = 0.5$ at $Re_c = 5\,\text{M}$ and $C_L^{\text{shape 2}} = 0.4$ at $Re_c = 30\,\text{M}$ respectively. During the computation, the angle of attack α is iteratively adjusted by the solver to converge towards a target lift, after an initial convergence at constant α. In the considered range of computation, the lift increases linearly with the angle of attack, so that the geometry is assumed to be deformed linearly as well. The drag and incidence values are thus simply interpolated between the results obtained with the two shapes for each lift coefficient C_L in the polar,

$$C_D^{\text{aeroelastic}} = f\, C_D|_{\text{shape 1}} + (1-f)\, C_D|_{\text{shape 2}}, \tag{30}$$

$$\alpha^{\text{aeroelastic}} = f\, \alpha|_{\text{shape 1}} + (1-f)\, \alpha|_{\text{shape 2}}, \tag{31}$$

$$\text{with } f = \left(C_L - C_L^{\text{shape 2}}\right) / \left(C_L^{\text{shape 1}} - C_L^{\text{shape 2}}\right).$$

Figs. 14 & 15 present the lift and drag coefficients as functions of the angle of attack for all four models and the NTF measurements, for $Re_c = 5\,\text{M}$ and $Re_c = 30\,\text{M}$.

Fig. 14 illustrates the lift overprediction of the models compared to the experiment, which is reduced with the RSMs, and more particularly with the EB-RSM. Indeed, in the low-*Re* case at $\alpha = 1.67°$, the relative error is of 11 % for the Spalart-Allmaras model, while it is of 9 % and 7 % for the ω-based RSMs and the EB-RSM respectively. Similarly, in the high-*Re* case, at $\alpha = 1.13°$, the relative error of 15 % for the Spalart-Allmaras model goes down to 12 % for the EB-RSM. Note that since the wind-tunnel measurements include wall-corrections, it is assumed that the experimental angles of attack are globally free from the influence of the wind-tunnel.

As seen in Fig. 15(a), the models overestimate the drag by 12 % at $Re_c = 5\,\text{M}$. The relative error is increased to 16 % for the SSG-ω-Aup model, as expected from the flat plate benchmark. Indeed, its systematic overprediction of the skin friction observed in Sec. 3 leads to an extra friction drag. For the high-*Re* case, Fig. 15(b), the same conclusions can be drawn, with an average relative error of 9 % for the Spalart-Allmaras and the SSG/LRR-ω models, increased to 12 % for the SSG-ω-Aup model. The EB-RSM here stands out from the others, as for the lift coefficient in Fig. 14(b), and improves the drag prediction with a relative error below 8 % to reference.

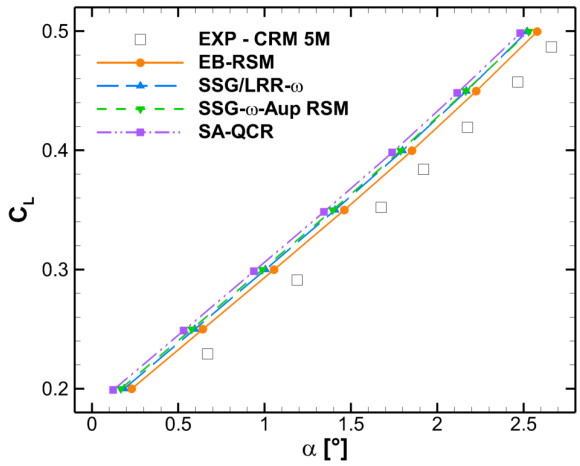

(a) $Re_c = 5\,\text{M}$

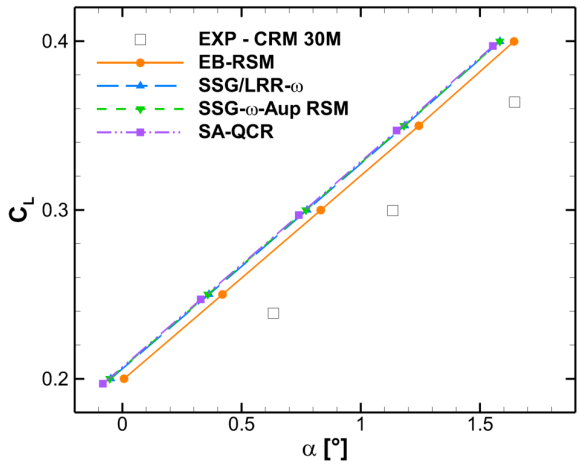

(b) $Re_c = 30\,\text{M}$

Figure 14: Lift coefficient on the CRM

The drag polars plotted in Figs. 16(a) & 17(a) show the evolution of drag with lift

$$C_D = C_{D,0} + C_{D,L}\,(C_L) \tag{32}$$

where $C_{D,0}$ is the drag remaining in zero-lift conditions and $C_{D,L}$ the drag due to lift, which includes the induced drag and the lift-dependent parts of friction, form and wave drags. Drag polars make it possible to distinguish the zero-lift drag $C_{D,0}$, corresponding essentially to the constant parts of the friction and form drags that appears as a lateral offset in the figures, from $C_{D,L}$ regardless of the angle of attack. Note that the value of $C_{D,0}$ is not computed for the models but only extrapolated.

All the models overpredict the drag, and mostly the friction drag according to the Skåre & Krogstad benchmark in previous section, where an overprediction of the skin friction coefficient was observed with all models. However, the increase of drag with lift is underpredicted, resulting in the total drag being less overpredicted for the highest values of C_L. It can be observed that the Spalart-Allmaras model better predicts the zero-lift drag compared to the Reynolds-stress models for the low-*Re* case. In

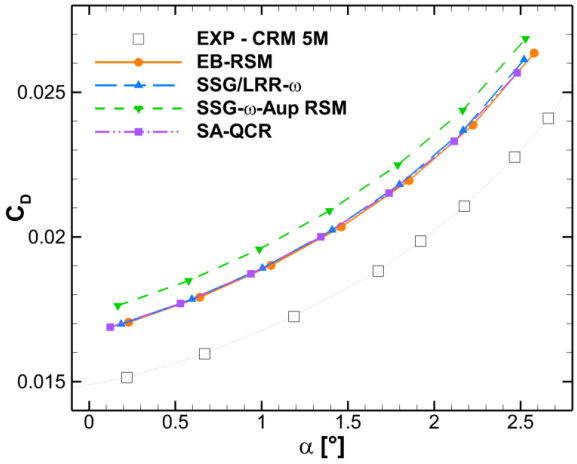

(a) $Re_c = 5\,\mathrm{M}$

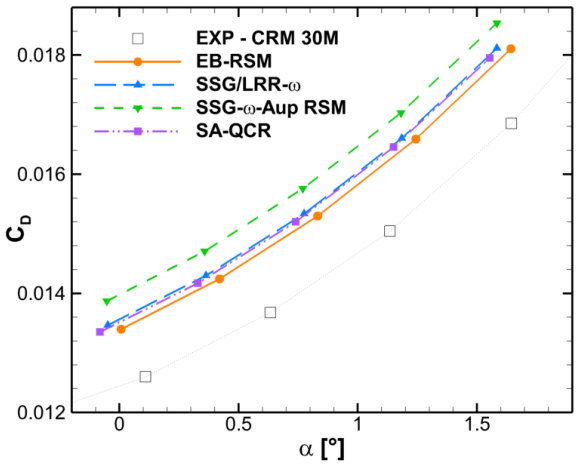

(b) $Re_c = 30\,\mathrm{M}$

Figure 15: Drag coefficient on the CRM

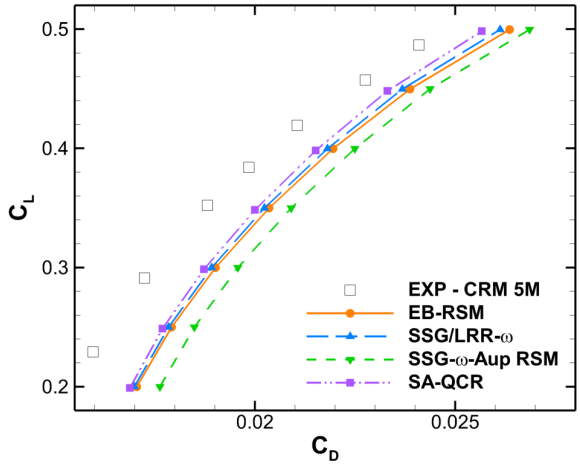

(a) $C_L = f(C_D)$

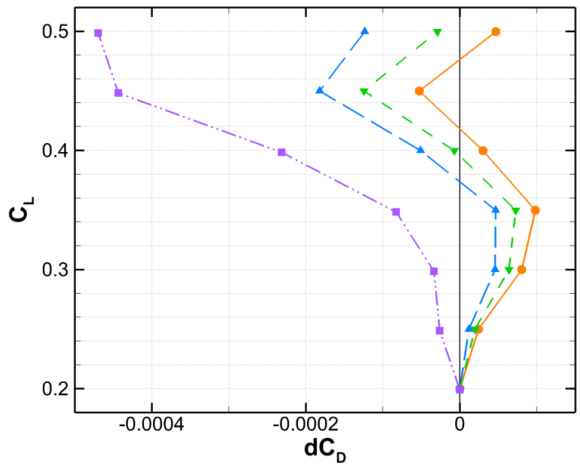

(b) Absolute error of the drag-due-to-lift

Figure 16: Drag polars on the CRM at $Re_c = 5\,\mathrm{M}$

particular, the shift of the SSG-ω-Aup model polar indicates that the extra friction observed in the flat plate benchmark mostly impacts $C_{D,0}$, hence the constant component of the friction drag. At $Re_c = 30\,\mathrm{M}$, the EB-RSM, the SSG/LRR-ω and the Spalart-Allmaras model almost coincide. For the EB-RSM, whereas $C_L(\alpha)$ and $C_D(\alpha)$ are improved, $C_D(C_L)$ is no better than for other models, reflecting a misprediction of the zero-lift drag.

In engineering applications, it is the response in drag to a given lift variation that is of interest, so that the drag polars are readjusted for a given polar point to compensate for the extra zero-lift drag due to wind-tunnel settings and aircraft excrescences, such as antenna and Pitot tubes. In the following, such readjusted drag polar is considered, with a reference point for the readjustment taken at $C_L = 0.2$. However, to focus on the error of drag due to lift, the absolute error of the readjusted drag polar to the experimental values is presented here rather than the readjusted drag polar itself. Hence, Figs. 16(b) & 17(b) show the polar of the drag error, defined as

$$\mathrm{d}C_D = C_D - C_D^{\mathrm{exp}} - \left(C_D|_{C_L=0.2} - C_D^{\mathrm{exp}}|_{C_L=0.2}\right). \tag{33}$$

These figures highlight the better $C_{D,L}$ prediction from the RSMs over the Spalart-Allmaras model, with an error that remains below one drag count ΔC_D[4] for the EB-RSM, and below $2\Delta C_D$ for the the ω-based RSMs. In particular in Fig. 16(b), the Spalart-Allmaras error at $C_L = 0.45$ for the low-Re case is reduced by 60 % with the SSG/LRR-ω model, by almost 75 % with the SSG-ω-Aup model and 90 % with the EB-RSM. The same conclusions apply to the high-Re case shown in Fig. 17(b), with however a reduced improvement, the EB-RSM still reducing the error by 30 %.

Note however that despite the engineering relevance of such plots, the improvement observed with the SSG-ω-Aup model should be considered with caution. Indeed, the polars presented here account for an exaggerated skin friction. Although it can

[4] a drag count is defined as $\Delta C_D = 10^{-4}$

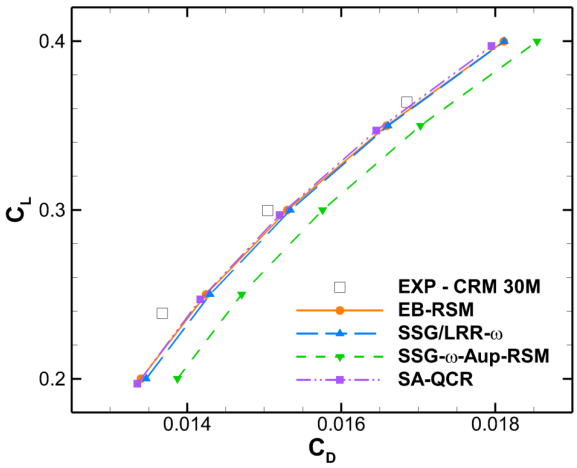

(a) $C_L = f(C_D)$

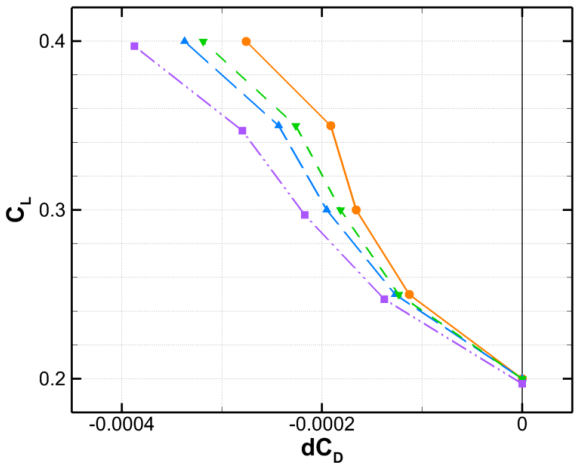

(b) Absolute error of the drag-due-to-lift

Figure 17: Drag polars on the CRM at $Re_c = 30\,\mathrm{M}$

be expected that a correction of the model regarding C_f would mostly affect the zero-lift drag $C_{D,0}$ due to its offset nature as observed on both the flat plate (Fig. 3) and the CRM, it may alter more globally the behaviour of the model.

4.2.2. *Pressure coefficient*

The pressure coefficient distribution have been computed on the deflected geometries, at the corresponding lift coefficients. Fig. 18 shows the C_p-distribution for both Reynolds numbers at three different spanwise positions, respectively close to the fuselage (dimensionless spanwise coordinate $\eta = y/s = 0.201$, with s the span), at the middle of the wing ($\eta = 0.502$) and close to the wing tip ($\eta = 0.846$).

The predictions of the RSMs are globally close to the Spalart-Allmaras model and to the reference. This can be expected from the fact that the results are here compared at matching lift coefficients. However, the corresponding angles of attack, gathered in Table 4, differ and are improved by the RSMs, in line with the lift polars (Fig. 14). The EB-RSM yields the closest α, with relative errors of 6 % for the low-*Re* case and 15 % for the high-*Re* one, while they are of 10 % and 19 % respectively with the Spalart Allmaras model.

Table 4: Angles of attack yielding the target C_L

	$Re_c = 5\,\mathrm{M}$ $C_L = 0.5$	$Re_c = 30\,\mathrm{M}$ $C_L = 0.4$
EXP	2.75°	1.92°
EB-RSM	2.58°	1.64°
SSG-ω-Aup RSM	2.53°	1.58°
SSG/LRR-ω RSM	2.52°	1.58°
SA-QCR	2.48°	1.55°

In the present comparison at given C_L, the models still tend to underestimate the aerodynamic load upstream of the shock wave and overestimate it downstream. This is especially visible for the three stations at $Re_c = 30\,\mathrm{M}$, in Figs. 18(b), (d) & (f).

The largest differences among models are located at the shock, the EB-RSM returning a shock position closest to the experiment for most of the considered stations, for both Reynolds numbers. The comparison with the experiments is however more difficult for some positions in the vicinity of the shock wave, due to the coarse resolution of the pressure probes, particularly at $\eta = 0.502$, where the supersonic flow upstream of the shock is barely measured.

A major contributor to the discrepancies between CFD and experiment is the depression occurring after the shock on the suction side, characterized by a 'rebound' on C_p, and largely overpredicted by models. This rebound grows from negligible at the body side into a second shock towards the wing tip. The rebound is amplified at high-*Re*, the depression becoming stronger than the leading edge depression at the wing tip in Fig. 18(f). It can be noted that the reduction of this overprediction for both cases follows the ranking of the models observed in Table 4, the EB-RSM yielding the smallest overprediction of the rebound and thus being the closest to the experiment.

4.2.3. *Conclusions on the CRM case*

Both the the drag polars and pressure-coefficient distributions demonstrated the improved accuracy of the Reynolds-stress models on an industrial aeronautical application compared to today's reference model in the industry, the Spalart-Allmaras model.

Despite the ω-equation being supposed to improve mild APG flow predictions, the computations on the CRM show here that the best results are achieved with the EB-RSM, relying on the ε-equation and a near-wall modeling. The SSG-ω-Aup model is however penalized by the overprediction of the skin friction, as already observed on the flat plate.

5. Conclusions

This study aimed at assessing the relevance of second-moment closures of the RANS equation to aeronautical applications. Three Reynolds-stress models that differ in their near-wall modeling and in their length-scale providing equation, namely the

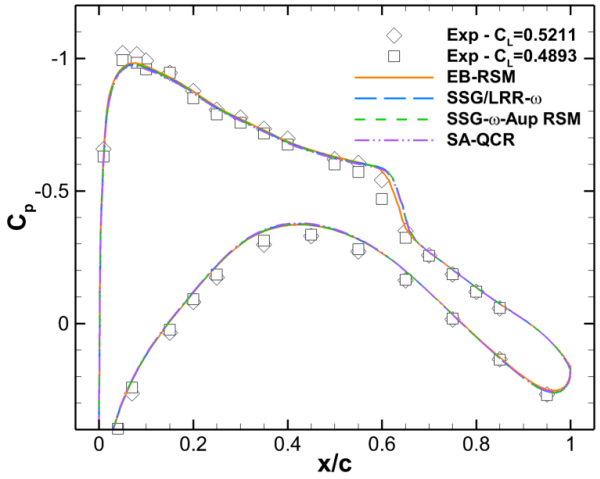

(a) $Re = 5\,\mathrm{M}$, $\eta = 0.201$

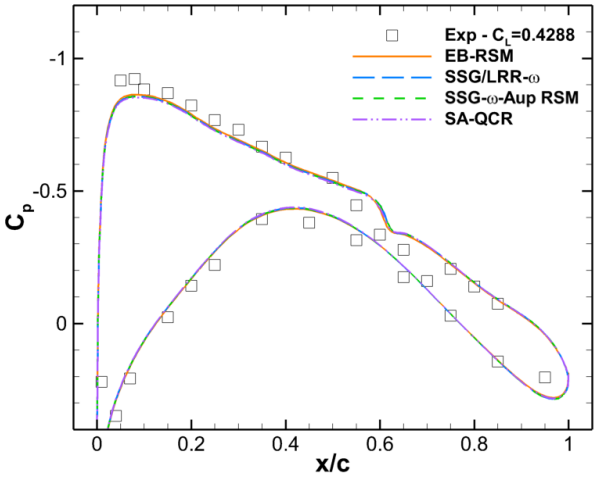

(b) $Re = 30\,\mathrm{M}$, $\eta = 0.201$

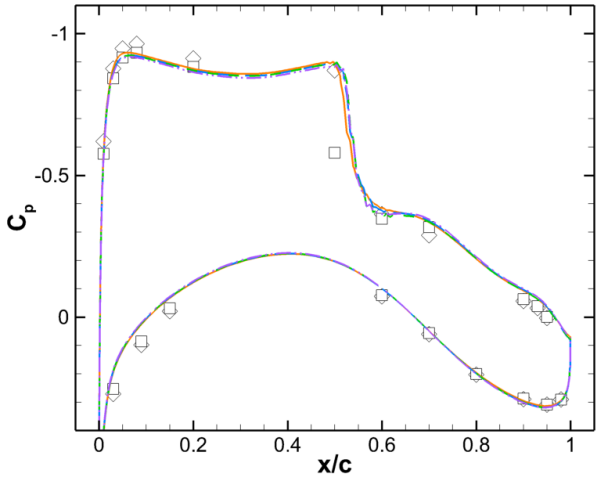

(c) $Re = 5\,\mathrm{M}$, $\eta = 0.502$

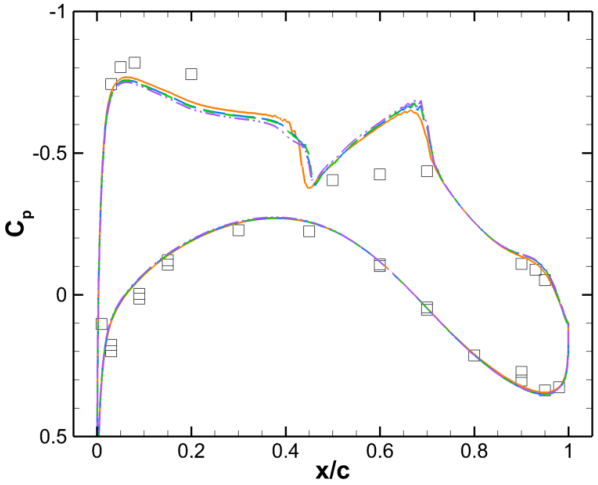

(d) $Re = 30\,\mathrm{M}$, $\eta = 0.502$

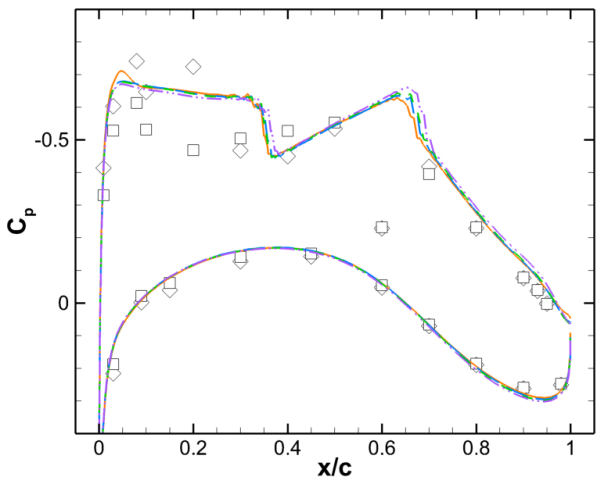

(e) $Re = 5\,\mathrm{M}$, $\eta = 0.846$

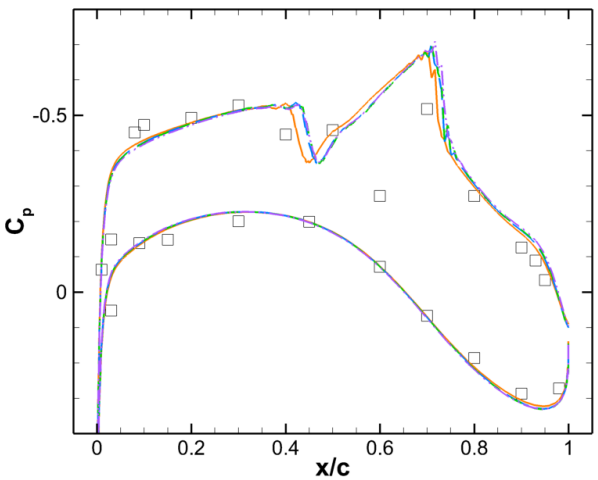

(f) $Re = 30\,\mathrm{M}$, $\eta = 0.846$

Figure 18: Pressure coefficients on the CRM

EB-RSM, the SSG/LRR-ω RSM and the SSG-ω-Aup RSM, were assessed on two academic test cases, a flat plate case and the Skåre & Krogstad case (Skåre and Krogstad, 1994) providing an APG flow at equilibrium, and one application case, the CRM aircraft case, against the Spalart-Allmaras model and empirical, DNS and experimental data.

The academic cases highlighted the fundamental differences between the models, regarding integral quantities and profiles in the boundary layer. In particular, the turbulence budgets in the flat plate test case demonstrated the effectiveness of near-wall modeling. In the CRM case, the RSMs also improved the predictions of pressure coefficients and the lift and drag polars with respect to the angle of attack. This should strengthen the attractiveness of these models in the aeronautical industry.

However, the Skåre & Krogstad test case showed that despite a satisfactory prediction of the boundary layer growth, the RSMs still need improvements regarding the skin friction prediction in strong APG flows. It also pointed out the shortcomings of the SSG-ω-Aup RSM which was not able to converge. Further assessments of Reynolds-stress models could also be carried out on different aeronautical cases, such as high-lift configurations and intake flow distortion predictions, where more complex flow phenomena can be expected, such as boundary layer-wake interactions and rotational flows.

Appendix A. SSG-ω-Aup RSM

Appendix A.1. Equations

Model equations:

$$\overline{\rho}\frac{\mathrm{D}R_{ij}}{\mathrm{D}t} = \overline{\rho}P_{ij} + \overline{\rho}D^{\nu}_{ij} + \overline{\rho}D^{T}_{ij} + \overline{\rho}\phi^{*}_{ij} - \overline{\rho}\varepsilon_{ij}, \tag{A.1}$$

$$\begin{aligned}\overline{\rho}\frac{\mathrm{D}\omega}{\mathrm{D}t} &= \gamma\overline{\rho}\frac{\omega}{k}P_k - \beta\overline{\rho}\omega^2 + \frac{\partial}{\partial x_j}\left(\overline{\mu}\frac{\partial\omega}{\partial x_j}\right)\\ &\quad + \frac{\partial}{\partial x_l}\left(\sigma_\omega\frac{\overline{\rho}k}{\omega}\frac{\partial\omega}{\partial x_l}\right) + 2\left(1-F_1\right)\frac{\sigma^{(\varepsilon)}_{\omega}}{\omega}\frac{\partial k}{\partial x_j}\frac{\partial\omega}{\partial x_j},\end{aligned} \tag{A.2}$$

Turbulent transport:

$$D^{T}_{ij} = \frac{\partial}{\partial x_l}\left(\frac{2}{3}\frac{C_s}{\beta^*}\nu_t\frac{\partial R_{ij}}{\partial x_l}\right), \tag{A.3}$$

$$\nu_t = f_w \min\left[\frac{k}{\omega}\,;k_0^{+3/2}\kappa\sqrt{k}y\right], \tag{A.4}$$

Velocity pressure-gradient correlation:

$$\phi^{*}_{ij} = f_b\,\phi^{SSG}_{ij} + (1-f_b)\,\phi^{w}_{ij}, \tag{A.5}$$

$$\begin{aligned}\phi^{SSG}_{ij} &= -\left(C_1\varepsilon + C^{*}_1P_k\right)b_{ij}\\ &\quad + C_2\varepsilon\left(b_{il}b_{jl} - \frac{1}{3}b_{mn}b_{mn}\delta_{ij}\right)\\ &\quad + \left(C_3 - C^{*}_3\sqrt{b_{mn}b_{mn}}\right)kS^{*}_{ij}\\ &\quad + C_4k\left(b_{il}S_{jl} + b_{jl}S_{il} - \frac{2}{3}b_{mn}S_{mn}\delta_{ij}\right)\\ &\quad + C_5k\left(b_{il}\Omega_{jl} + b_{jl}\Omega_{il}\right),\end{aligned} \tag{A.6}$$

$$\phi^{w}_{ij} = -5\frac{\varepsilon}{k}\left(R_{ik}n_jn_k + R_{jk}n_in_k - \frac{1}{2}R_{kl}n_kn_l\left(n_in_j + \delta_{ij}\right)\right), \tag{A.7}$$

$$b_{ij} = \frac{R_{ij}}{2k} - \frac{1}{3}\delta_{ij}, \qquad S_{ij} = \frac{1}{2}\left(\frac{\partial\widetilde{U}_i}{\partial x_j} + \frac{\partial\widetilde{U}_j}{\partial x_i}\right), \tag{A.8}$$

$$S^{*}_{ij} = S_{ij} - \frac{1}{3}S_{kk}\delta_{ij}, \qquad \Omega_{ij} = \frac{1}{2}\left(\frac{\partial\widetilde{U}_i}{\partial x_j} - \frac{\partial\widetilde{U}_j}{\partial x_i}\right), \tag{A.9}$$

Dissipation rate:

$$\varepsilon_{ij} = f_b\,\frac{2}{3}\varepsilon\delta_{ij} + (1-f_b)\,\frac{R_{ij}}{k}\varepsilon, \tag{A.10}$$

$$\varepsilon = f_\varepsilon \max\left(\beta^{*}k\omega\,;\left(\frac{k}{k_0^{+}}\right)^{3/2}\frac{1}{\kappa y}\right), \tag{A.11}$$

Blending functions:

$$f_b = 1 - \exp\left(-\left[\frac{1}{225}\left(\frac{\omega y^2}{\nu} - \frac{6}{\beta^{(\omega)}}\right)\right]^2\right), \tag{A.12}$$

$$f_w = 1 - \exp\left(-\left[\frac{\omega y^2}{250\nu}\right]^{2.5}\right), \tag{A.13}$$

$$f_\varepsilon = \frac{5}{18} + \frac{13}{18}\tanh\left(\left[\frac{y}{42}\left(\frac{\omega k}{\nu^3}\right)^{1/4}\right]^3\right), \tag{A.14}$$

$$F_1 = \tanh\left(\arg_1^4\right), \tag{A.15}$$

$$\arg_1 = \min\left[\max\left(\frac{\sqrt{k}}{\beta^*\omega y}; \frac{500\overline{\mu}}{\overline{\rho}\omega y^2}\right); \frac{4\sigma_\omega^{(\varepsilon)} k}{\mathrm{CD}_{k\omega} y^2}\right], \tag{A.16}$$

$$\mathrm{CD}_{k\omega} = \max\left(\frac{2\sigma_\omega^{(\varepsilon)}}{\omega}\frac{\partial k}{\partial x_j}\frac{\partial \omega}{\partial x_j}; 10^{-20}\right). \tag{A.17}$$

Appendix A.2. Coefficients

The coefficients in the BSL ω-equation are blended according to $c = F_1\, c^{(\omega)} + (1 - F_1)\, c^{(\varepsilon)}$

$$\gamma^{(\omega)} = 5/9; \quad \beta^{(\omega)} = 0.075; \quad \sigma_\omega^{(\omega)} = 0.605;$$
$$\gamma^{(\varepsilon)} = 0.664; \quad \beta^{(\varepsilon)} = 0.0828; \quad \sigma_\omega^{(\varepsilon)} = 0.65; \quad \beta^* = 0.09$$

$$C_s = 0.22; \quad k_0^+ = 3.118556; \quad \kappa = 0.41$$
$$C_1 = 3.4; \quad C_1^* = 1.8; \quad C_2 = 4.2; \quad C_3 = 0.8;$$
$$C_3^* = 1.30; \quad C_4 = 1.25; \quad C_5 = 0.40$$

References

Aupoix, B., 2012. Improving the coupling of the Speziale, Sarkar and Gatski differential Reynolds stress model with an ω scale equation. Technical Report 13929. ONERA. Unpublished.

Billard, F., 2012. Development of a robust elliptic-blending turbulence model for near-wall, separated and buoyant flows. Ph.D. thesis. University of Manchester.

Catris, S., Aupoix, B., 2000. Towards a calibration of the length-scale equation. Int. J. Heat Fluid Fl. 21, 606–613.

Cécora, R.D., Radespiel, R., Eisfeld, B., Probst, A., 2015. Differential Reynolds-stress modeling for aeronautics. AIAA Journal 53, 739–755.

Chalot, F., 2004. Industrial aerodynamics, in: Stein, E., de Borst, R., Hughes, T.J.R. (Eds.), Encyclopedia of Computational Mechanics. John Wiley & Sons, Ltd.. volume 3: Fluids. chapter 12.

Clauser, F.H., 1954. Turbulent boundary layers in adverse pressure gradients. J. Aeronaut. Sci. 21, 91–108.

Durbin, P.A., 1991. Near-Wall Turbulence Closure Modeling Without "Damping Functions". Theor. Comput. Fluid Dyn. 3, 1–13.

Eisfeld, B., 2004. Implementation of Reynolds stress models into the DLR-FLOWer code. Technical Report. DLR Institute of Aerodynmaics and Flow Technology. Unpublished.

Eisfeld, B., Rumsey, C.L., Togiti, V., 2016. Verification and validation of a second-moment-closure model. AIAA J. 54, 1524–1541.

Huang, P.G., Bradshaw, P., 1995. Law of the wall for turbulent flows in pressure gradients. AIAA J. 33, 624–632.

Keye, S., Gammon, M., 2016. Development of Deformed CAD Geometries of NASA's Common Research Model for the Sixth AIAA CFD Drag Prediction Workshop, in: 34th AIAA Applied Aerodynamics Conference, p. 3431.

Knopp, T., Novara, M., Schanz, D., Geisler, R., Philipp, F., Schroll, M., Willert, C., Schröder, A., 2018. Modification of the SSG/LRR-ω RSM for Turbulent Boundary Layers at Adverse Pressure Gradient with Separation Using the New DLR VicToria Experiment, in: Symposium der Deutsche Gesellschaft für Luft-und Raumfahrt, Springer. pp. 80–89.

Knopp, T., Reuther, N., Novara, M., Schanz, D., Schülein, E., Schröder, A., Kähler, C.J., 2021. Experimental analysis of the log law at adverse pressure gradient. J. Fluid Mech. 918.

Launder, B.E., Reece, G.J., Rodi, W., 1975. Progress in the development of a Reynolds-stress turbulence closure. J. Fluid Mech. 68, 537–566.

Mallet, M., 1985. A finite element method for computational fluid dynamics. Ph.D. thesis. Stanford University.

Manceau, R., 2015. Recent progress in the development of the Elliptic Blending Reynolds-stress model. Int. J. Heat Fluid Fl. 51, 195–220. doi:10.1016/j.ijheatfluidflow.2014.09.002.

Manceau, R., Hanjalić, K., 2002. Elliptic Blending Model: A New Near-Wall Reynolds-Stress Turbulence Closure. Phys. Fluids 14, 744–754. doi:10.1063/1.1432693.

Menter, F.R., 1994. Two-equation eddy-viscosity turbulence models for engineering applications. AIAA J. 32, 1598–1605.

Morkovin, M.V., 1962. Effects of compressibility on turbulent flows. Mécanique de la Turbulence 367, 380.

Morsbach, C., Franke, M., di Mare, F., 2015. Application of a low Reynolds differential Reynolds stress model to a compressor cascade tip-leakage flow, in: Differential Reynolds Stress Modeling for Separating Flows in Industrial Aerodynamics. Springer, pp. 1–17.

Nickels, T.B., 2004. Inner scaling for wall-bounded flows subject to large pressure gradients. J. Fluid Mech. 521, 217–239.

Paysant, R., 2016. Amélioration de la modélisation des écoulements turbulents. Technical Report. ISAE-ENSICA.

Rotta, J.C., 1951. Statistische Theorie nichthomogener Turbulenz. Z. Phys. 129, 547–572.

Schlatter, P., Li, Q., Brethouwer, G., Johansson, A.V., Henningson, D.S., 2010. Simulations of spatially evolving turbulent boundary layers up to $Re_\theta = 4{,}300$. Int. J. Heat Fluid Fl. 31, 251–261.

Schlichting, H., 1979. Boundary-Layer Theory. 7th edition ed., McGraw-Hill.

Schoenherr, K.E., 1932. Resistance of flat surfaces moving through a fluid. Soc. Nav. Arch. and Marine Eng. Trans. 40, 279–313.

Skåre, P.E., Krogstad, P.Å., 1994. A turbulent equilibrium boundary layer near separation. J. Fluid Mech. 272, 319–348.

Spalart, P.R., 2000. Strategies for turbulence modelling and simulations. Int. J. Heat Fluid Fl. 21, 252–263.

Speziale, C.G., Sarkar, S., Gatski, T.B., 1991. Modeling the pressure-strain correlation of turbulence: an invariant dynamical system approach. J. Fluid Mech. 227, 245–272.

Tinoco, E.N., Brodersen, O.P., Keye, S., Laflin, K.R., Feltrop, E., Vassberg, J.C., Mani, M., Rider, B., Wahls, R.A., Morrison, J.H., Hue, D., Roy, C.J., Mavriplis, D.J., Murayama, M., 2018. Summary Data from the Sixth AIAA CFD Drag Prediction Workshop: CRM Cases. J. Aircraft 55, 1352–1379. doi:10.2514/1.C034409.

Togiti, V., Eisfeld, B., 2015. Assessment of g-equation formulation for a second-moment Reynolds stress turbulence model, in: 22nd AIAA Computational Fluid Dynamics Conference, p. 2925.

Togiti, V., Eisfeld, B., Brodersen, O., 2014. Turbulence model study for the flow around the NASA common research model. J. Aircraft 51, 1331–1343.

Vassberg, J., Dehaan, M., Rivers, M., Wahls, R., 2008. Development of a common research model for applied CFD validation studies, in: 26th AIAA applied aerodynamics conference, p. 6919.

Wilcox, D.C., 2006. Turbulence Modeling for CFD. Third ed., DCW industries, Inc., La Cañada, California.